Journal of Cosmology and Astroparticle Physics
An IOP and SISSA journal

Received: July 23, 2025
Revised: October 1, 2025
Accepted: October 4, 2025
Published: November 7, 2025

Braneworld dark energy in light of DESI DR2

Swagat S. Mishra[a,b] **William L. Matthewson**[c] **Varun Sahni**[b] **Arman Shafieloo**[c,d] **and Yuri Shtanov**[e]

[a] *School of Physics and Astronomy, University of Nottingham, Nottingham, NG7 2RD, U.K.*
[b] *Inter-University Centre for Astronomy and Astrophysics, Post Bag 4, Ganeshkhind, Pune 411 007, India*
[c] *Korea Astronomy and Space Science Institute (KASI), 776 Daedeok-daero, Yuseong-gu, Daejeon 34055, Korea*
[d] *KASI Campus, University of Science and Technology, 217 Gajeong-ro, Yuseong-gu, Daejeon 34113, Korea*
[e] *Bogolyubov Institute for Theoretical Physics, Metrologichna St. 14-b, Kiev 03143, Ukraine*

E-mail: swagat.mishra@nottingham.ac.uk, willmatt4th@kasi.re.kr, varun@iucaa.in, shafieloo@kasi.re.kr, shtanov@bitp.kyiv.ua

Abstract: Recent observational results from the DESI collaboration reveal tensions with the standard ΛCDM model and favour a scenario in which dark energy (DE) decays over time. The DESI DR2 data also suggest that the DE equation of state (EoS) may have been phantom-like ($w < -1$) in the past, evolving to $w > -1$ at present — implying a recent crossing of the phantom divide at $w = -1$.

Scalar field models of DE naturally emerge in ultraviolet-complete theories such as string theory, which is typically formulated in higher dimensions. In this work, we investigate a broad class of *thawing scalar field models* — including the simple quadratic, quartic, exponential, symmetry-breaking and axion potentials — propagating on a (4+1)-dimensional ghost-free phantom braneworld, and demonstrate that their effective EoS exhibits a phantom-divide crossing. Alongside the Hubble parameter and EoS of DE, we also analyse the evolution of the *Om* diagnostic, and demonstrate that the time dependence of these quantities is in excellent agreement with the DESI DR2 observations. Furthermore, we perform a comprehensive parameter estimation using Markov Chain Monte Carlo sampling, and find that the χ^2 values for all our models are remarkably close to that of the widely used CPL parametrisation — indicating that our models fit the data very well.

Keywords: cosmology with extra dimensions, dark energy theory, extra dimensions, modified gravity

ArXiv ePrint: 2507.07193

https://doi.org/10.1088/1475-7516/2025/11/018

JCAP11(2025)018

Contents

1 Introduction

Ever since the remarkable serendipitous discovery of cosmic acceleration [1, 2], the physical nature of dark energy (DE) has remained elusive and somewhat of an enigma. Although a cosmological constant (CC) with $T_{ik} = \Lambda\, g_{ik} \;\Rightarrow\; p = -\rho$ provides a good fit to most of the data, if CC is to be associated with the vacuum energy then its extremely small value $\rho_{\rm vac} \sim 10^{-47}\,{\rm GeV}^4$, suggested by observations, appears to be difficult to reconcile with expectations from fundamental physics and quantum field theory [3, 4]. Alternatives to the cosmological constant that can induce late-time acceleration have been actively explored in the literature. These usually involve modifications either to the right-hand side or the left-hand side of the Einstein equations $G_{ik} = 8\pi G\, T_{ik}$. Early candidates for the former

JCAP11(2025)018

include scalar fields with appropriately chosen potentials [5, 6], while to the latter belong late-time modifications to Einstein's general relativity (GR); see [7–19] for extensive reviews on the subject.

In the absence of terrestrial (laboratory) tests of DE, the key to understanding its properties lies in a comprehensive analysis of cosmological data sets. In this connection, model-independent techniques [20] applied to observational data provide an attractive route to discerning the properties of DE at a deeper level. To this category belong the popular CPL ansatz [21, 22] for the DE equation of state (EoS), defined as

$$w(a) = w_0 + w_a(1-a) = w_0 + w_a\left(\frac{z}{1+z}\right), \tag{1.1}$$

and the Om diagnostic [23–25] which provides a null test of ΛCDM [1]

$$Om(z) = \frac{h^2(z)-1}{(1+z)^3-1}, \qquad h(z) \equiv \frac{H(z)}{H_0}. \tag{1.2}$$

Interestingly, when applied to the DESI DR2 data [26–28], both methods suggest that cosmic acceleration may be slowing down at the present epoch [29–33]. What is even more surprising is the fact that a model-independent analysis of several data sets indicates that DE passed through a recent *phantom* phase when its EoS dropped below -1 [29]. If these results stand up to further scrutiny [34–37], then they appear to imply that DE crossed the phantom divide in its recent past, since $w(z) < -1$ at $z \gtrsim 1$ and $w(z) > -1$ at $z \lesssim 1$. (Tension with the ΛCDM model stands at between 2σ and 3σ confidence levels [37–43].)

Since the DESI results point towards decaying DE whose EoS increases with time, it is instructive to work with *thawing models*[2] of dynamical DE [44]. Although these models cannot accommodate phantom-crossing in GR, they do so quite easily when propagating on a higher dimensional braneworld. Indeed, it is well known that a *phantom brane* with a brane tension has an effective EoS which is lower than -1 [45–48]. In fact, the lowering of the dark energy EoS relative to its GR value is an important generic feature of phantom brane cosmology. In the present analysis, we assume that the brane tension (vacuum energy) is zero, and that any effective vacuum energy at a given epoch arises from an ultra-light scalar field that has not yet relaxed to its vacuum state. (This is in line with the customary assumption made in most scalar-field (quintessence) models of DE in the literature [49].) Such a scalar field propagating on the brane will initially have an effective DE EoS $w < -1$, when the field $\phi(t)$ is frozen to its initial value. At late times, when ϕ begins rolling down its potential,[3] the effective DE EoS crosses the phantom divide and increases to $w > -1$. (Dynamical DE models have also been discussed in [50–64] in the context of DESI DR2.)

[1] We use the notation $h(z) \equiv H(z)/H_0$, as defined in eqs. (1.2) and (2.2), throughout this paper, where $h(z)$ is a variable that changes with redshift. However, in order to avoid confusion, it is worth pointing out that often the letter h stands for $h \equiv H_0$ $(100\ \mathrm{km/(s\,Mpc)})^{-1}$ in the cosmology literature, where h is a constant, and does not vary with redshift.

[2] Thawing models complement *freezing models* in which the DE EoS decreases with time and tends towards a more negative value in the asymptotic future [44].

[3] An ultra-light scalar field remains frozen to its initial value as long as the 'friction term' $3H\dot{\phi}$ is larger than the 'force' term $V_{,\phi}$ in the equation of motion $\ddot{\phi} + 3H\dot{\phi} + V_{,\phi} = 0$. As the universe expands, H decreases allowing $V_{,\phi}$ to influence the motion of ϕ, which leads to growth in the EoS $w(t)$ at late times. This is also

JCAP11(2025)018

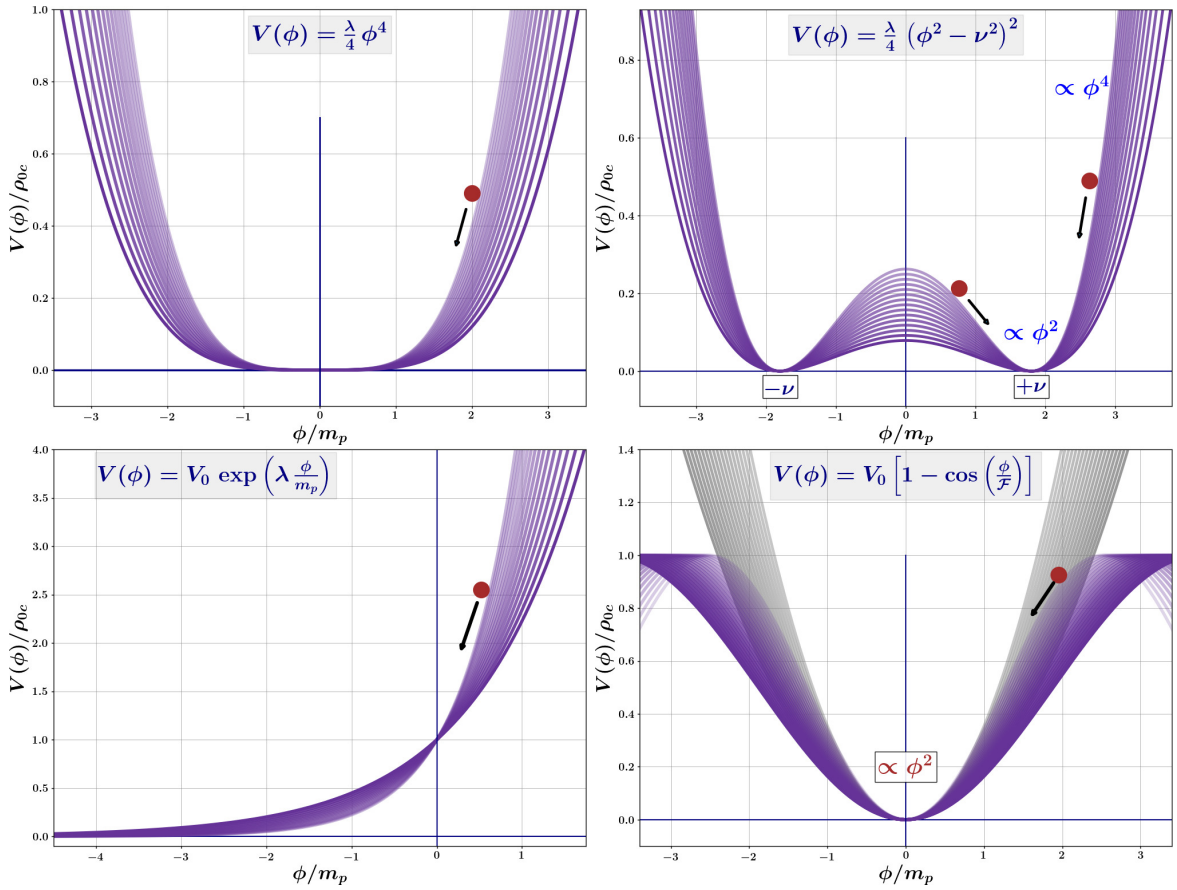

Figure 1. Schematic plots of different potentials considered in this work. *Top-left panel* shows the quartic potential (1.4) for different values of λ. *Top-right panel* shows the symmetry-breaking potential (1.5) for fixed value of ν, and different values of λ. *Bottom-left panel* shows the exponential potential (1.6) for fixed value of V_0, and different values of λ. *Bottom-right panel* shows the pseudo Nambu-Goldstone boson/axion potential (1.7) for different values of the axion mass (3.10) (the quadratic approximation (3.9) is displayed in light-gray curves).

In this paper, we demonstrate that the following scalar-field potentials residing on the brane give rise to dynamical dark energy with an EoS which crosses the phantom divide, in broad agreement with the DESI DR2 results. The potentials are illustrated in figure 1.

1. An ultra-light scalar field with negligible self-interaction, described by the quadratic potential [4]

$$V(\phi) = \frac{1}{2}m^2\phi^2 \,. \tag{1.3}$$

true if the effective DE EoS drops below $w = -1$ in the recent past, because the total effective density of the not-yet-DE-dominated universe, nevertheless, keeps dropping, and therefore H keeps decreasing, allowing $V_{,\phi}$ to influence the late-time motion of ϕ.

[4]Note that the quadratic potential can be realised as a limiting case of the symmetry-breaking potential (1.5) and the axion potential (1.7).

JCAP11(2025)018

2. A massless scalar field with a quartic self-interaction

$$V(\phi) = \frac{\lambda}{4}\,\phi^4\,. \tag{1.4}$$

3. The symmetry-breaking potential

$$V(\phi) = \frac{\lambda}{4}\,\left(\phi^2 - \nu^2\right)^2\,. \tag{1.5}$$

4. An exponential potential

$$V(\phi) = V_0\,\exp\left(\lambda\,\frac{\phi}{m_p}\right). \tag{1.6}$$

5. A pseudo Nambu-Goldstone boson with an axion potential [49]

$$V(\phi) = V_0\left[1 - \cos\left(\frac{\phi}{\mathcal{F}}\right)\right]\,. \tag{1.7}$$

   A similar potential $V(\phi) = V_0 \cos\left(\frac{\phi}{\mathcal{M}}\right)$ has been discussed [5] in the context of the string theory axion [67] and tested against observations in [65].

6. And finally, an asymptotically flat (plateau) potential

$$V(\phi) = V_0\,\tanh^2\left(\lambda\,\frac{\phi}{m_p}\right). \tag{1.8}$$

Our paper is organised as follows. In section 2, we introduce the braneworld model employed in our study and present the cosmological equations that are solved numerically. Section 3 details the numerical solutions and the resulting behaviour of the effective dark energy for various scalar-field potentials, while section 4 is dedicated to a comprehensive parameter estimation for these potentials using Markov Chain Monte Carlo (MCMC) sampling against the publicly available DESI DR2 data. Sections 3 and 4 constitute the core of this work. We discuss the implications of our results in section 5. Appendix A is dedicated to a discussion on the existence of a pole in the effective EoS of DE on the phantom brane at a higher redshift. Appendix B discusses the evolution of other physical quantities in our models. Finally, details for a specific asymptotically flat scalar field potential are provided in appendix C.

2 Cosmological equations on the phantom brane

The phantom braneworld model, detailed in [45], features a phantom-like effective EoS for dark energy, characterised by $w_{\rm eff} < -1$ [46]. The generic action for this cosmological

[5] An interesting property of this potential is that it becomes negative at late times which can cause the universe to stop expanding and begin to contract [65]. More general axion-like potentials have also been discussed in [66] and references therein. However, in our analysis, the axion potential is always positive semi-definite, i.e. $V(\phi) \geq 0$, as can be inferred from eq. (1.7).

JCAP11(2025)018

braneworld model, originally suggested by Collins and Holdom [68] (and independently by Shtanov [69]), also known as the Dvali-Gabadadze-Porrati (DGP) model [70], reads [6] [68–70]

$$S = M_p^3 \int_{\text{bulk}} (\mathcal{R} - 2\Lambda_{\text{b}}) + \frac{m_p^2}{2} \int_{\text{brane}} (R - 2\Lambda) + \int_{\text{brane}} L_{\text{m}} \,. \tag{2.1}$$

This model represents a simple general-relativistic action in the five-dimensional bulk (with scalar curvature $\mathcal{R}$) and on the four-dimensional brane (with scalar curvature R), with matter confined only to the brane and described by the Lagrangian L_{m}. Integrations over the bulk and brane are taken with the corresponding natural volume elements. The universal constants $m_p = 1/\sqrt{8\pi G}$ and M_p play the role of the Planck masses on the brane and in the bulk space, respectively. The symbols Λ and Λ_{b} denote, respectively, the cosmological constants on the brane and in the bulk, so that $m_p^2\Lambda$ is the brane tension from the five-dimensional bulk perspective.

This paper examines a braneworld model in which the cosmological constants associated with both the brane and the bulk are excluded, i.e. $\Lambda_{\text{b}} = \Lambda = 0$. It is postulated that there exists a mechanism that nullifies these constants in vacuum. Instead, any effective pseudo-vacuum energy present at a specific epoch is attributed to an ultra-light scalar field that has not yet reached its vacuum state. Cosmologically, this implies that the effective dark energy in the universe evolves due to two distinct effects: the braneworld dynamics and the time-dependent evolution of the ultra-light scalar field.

We consider the universe at relatively late times, that is, $z \ll 10^2$, for which the density of radiation can be safely ignored. The expansion rate on a phantom brane (which corresponds to the normal, ghost-free [71–73], branch of the DGP model [69, 74, 75]) filled with matter and a scalar field describing dynamical dark energy is then expressed as [45, 76]

$$h(z) \equiv \frac{H(z)}{H_0} = \sqrt{\Omega_{0m}(1+z)^3 + \frac{\rho_\phi}{3m_p^2H_0^2} + \Omega_{0\ell}} - \sqrt{\Omega_{0\ell}} \,, \tag{2.2}$$

where

$$\rho_\phi = \frac{1}{2}\dot{\phi}^2 + V(\phi) \tag{2.3}$$

is the energy density of the scalar field (regarded as a function of redshift), and

$$\Omega_{0m} = \frac{\rho_{0m}}{3m_p^2H_0^2} \,, \qquad \Omega_{0\ell} = \frac{1}{\ell^2 H_0^2} \,, \qquad \ell = \frac{m_p^2}{M_p^3} \,. \tag{2.4}$$

The Omega parameters obey the constraint that follows from the condition $h(0) = 1$:

$$\Omega_{0m} + \frac{\rho_{0\phi}}{3m_p^2H_0^2} - 2\sqrt{\Omega_{0\ell}} = 1 \,, \tag{2.5}$$

where $\rho_{0\phi}$ is the current value of ρ_ϕ. Note that $\Omega_{0\ell}$ is the new fundamental parameter in our model. It is associated with the presence of a fifth dimension (the bulk). Setting $\Omega_{0\ell} = 0$ in (2.2), one recovers the expansion rate in GR.

[6] We adopt the mostly-plus metric signature and work in natural units, setting $\hbar = c = 1$. In (2.1), we use the standard general-relativistic normalisation of the action on the brane, which differs by a factor of 1/2 from the normalisation used in [45, 69, 70].

JCAP11(2025)018

Constraints on the fundamental parameter ℓ from local gravitational physics are significantly weaker than those derived from cosmological observations, including those presented in this work. The presence of extra-dimensional gravity induces corrections to Newton's laws, potentially leading to observable anomalies within the Solar System. Notably, all planets would experience a uniform anomalous perihelion precession with a rate given by $\dot{\phi} = -3/4\ell$ [77]. The non-detection of this effect in observations imposes a lower bound on the fundamental length parameter, $\ell \gtrsim 0.26$ Gpc [78]. Another constraint, $\ell \gtrsim 0.32$ Gpc, arises from Lunar Laser Ranging experiments [79, 80].[7] In terms of the parameter $\Omega_{0\ell}$ defined in (2.4), this translates into an upper bound

$$\Omega_{0\ell} \lesssim 180\, h_{70}^{-2}\,, \tag{2.6}$$

where $h_{70} = H_0/\,(70\ \mathrm{km/(s\,Mpc)})$. This is several orders of magnitude larger than the typical best-fit values $\Omega_{0\ell} \simeq 0.013$ obtained in this work (see below).

From the perspective of general relativity, the effective dark energy density in our model is defined as

$$\rho_{\mathrm{DE}} = 3m_p^2 H_0^2 h^2 - \rho_m = \rho_\phi - 6m_p^2 H_0^2 \sqrt{\Omega_{0\ell}}\, h\,. \tag{2.7}$$

The second equality follows from eq. (2.2) by rearranging its terms and squaring both sides.

The scalar field respects the usual equation

$$\ddot{\phi} + 3H\dot{\phi} + V_{,\phi}(\phi) = 0\,, \tag{2.8}$$

where $V_{,\phi} = \mathrm{d}V/\mathrm{d}\phi$. According to our assumptions, the vacuum value for the scalar field potential is zero.

In this work, we integrate the above equations starting from an initial redshift of $z = 99$. This choice corresponds to a sufficiently early evolutionary epoch, while, at the same time, allowing us to neglect the contribution from radiation, which is subdominant at this and later epochs. The initial time derivative $\dot{\phi}$ of the scalar field is set to zero, and the initial value of ϕ is chosen so that the constraint eq. (2.5) is satisfied with $\Omega_{0m} = 0.315$. This value of Ω_{0m} is held fixed across all our simulations, while the remaining parameters are varied.

After the solutions are obtained, we can evaluate the deceleration parameter $q(z)$, the effective DE density relative to its present-epoch value $f_{\mathrm{DE}}(z)$ and the effective equation-of-state parameter $w_{\mathrm{DE}}(z)$ of DE using the following expressions:

$$q(z) \equiv -\frac{\ddot{a}}{a\,H^2} = \frac{h'(z)}{h(z)}\,(1+z) - 1\,, \tag{2.9}$$

$$f_{\mathrm{DE}}(z) \equiv \frac{\rho_{\mathrm{DE}}}{\rho_{0\mathrm{DE}}} = h^2(z)\left(\frac{1-\Omega_m(z)}{1-\Omega_{0m}}\right)\,, \tag{2.10}$$

$$w_{\mathrm{DE}}(z) = \frac{2\,q(z) - 1}{3\,(1-\Omega_m(z))}\,, \tag{2.11}$$

with

$$\Omega_m(z) = \Omega_{0m}\,\frac{(1+z)^3}{h^2(z)}\,. \tag{2.12}$$

[7] Our constant ℓ is equal to twice the length scale r_0 introduced and constrained in [77–80].

JCAP11(2025)018

It is worth noting that the effective EoS of DE on the phantom brane is known to exhibit a pole [45] at a redshift $z = z_p$ where $\Omega_m(z_p) = 1$, as can be seen from eq. (2.11). The existence of such a pole is purely a result of the effective description of DE, and does not correspond to an actual singularity in the system. See appendix A for a discussion on the location of the pole.[8]

By combining eqs. (2.2), (2.3), (2.8), (2.9), and (2.12), the effective EoS of DE (2.11) can be written as

$$w_{\rm DE}(z) = -1 - \left[\frac{\sqrt{\Omega_{0\ell}}\,\Omega_m(z) - \frac{1}{h(z)}\,\frac{\dot{\phi}^2}{3m_p^2H_0^2}}{(1-\Omega_m(z))\,\left(h(z)+\sqrt{\Omega_{0\ell}}\right)}\right], \tag{2.13}$$

which indicates that, at higher redshifts, when the scalar field is frozen at its initial value, i.e. $\dot{\phi} \simeq 0$, the EoS of DE is phantom like, satisfying $w_{\rm DE}(z) < -1$ (provided $\Omega_m \neq 1$, which is a pole, as noted above). The expression for the EoS of DE at the present epoch, $z = 0$, is given by

$$w_{\rm DE}(0) = -1 + \left[\frac{\Omega_{0\phi,{\rm KE}} - \Omega_{0m}\sqrt{\Omega_{0\ell}}}{(1-\Omega_{0m})\,\left(1+\sqrt{\Omega_{0\ell}}\right)}\right], \tag{2.14}$$

where $\Omega_{0\phi,{\rm KE}} \equiv \dot{\phi}_0^2/\left(3m_p^2H_0^2\right)$. Importantly, eq. (2.14) demonstrates that, at the present epoch, if $\Omega_{0\phi,{\rm KE}} > \Omega_{0m}\sqrt{\Omega_{0\ell}}$, then $w_{\rm DE} > -1$, ensuring the phantom-divide crossing at some intermediate epoch $z > 0$.

3 Dynamics of different DE models on the phantom brane

In this section, we discuss the dynamics of DE for the quadratic (1.3), quartic (1.4), symmetry-breaking (1.5), exponential (1.6) and axion (1.7) potentials as representatives of a broad class of simple thawing models in our braneworld scenario. While the plateau potential (1.8) also fits the data quite well, its best-fit parameters lead to an EoS of DE that resembles that of the quadratic potential (as well as the axion potential). Therefore we discuss it in the appendix C, in order to maintain a simpler presentation in the main text of the manuscript.

As discussed above, we set both the brane tension and the bulk cosmological constant to zero. In the limit $\Omega_{0\ell} \to 0$, our model reduces to that of a massive scalar field in General Relativity. In all plots appearing in this section, we fix the present-day dark energy density parameter to $\Omega_{0{\rm DE}} \equiv 1 - \Omega_{0m} = 0.685$, and investigate the effects of varying $\Omega_{0\ell}$ along with other parameters specific to the chosen scalar-field potentials.

3.1 Quadratic potential

We first turn our attention to the simple quadratic scalar-field potential (gray colour curves in bottom-right panel of figure 1), given by

$$V(\phi) = \frac{1}{2}\,m^2\phi^2\,, \tag{3.1}$$

where m is mass of the scalar field.

[8] See ref. [59] for the analysis of a coupled matter-quintessence model in GR which exhibits two poles in the effective EoS of DE.

JCAP11(2025)018

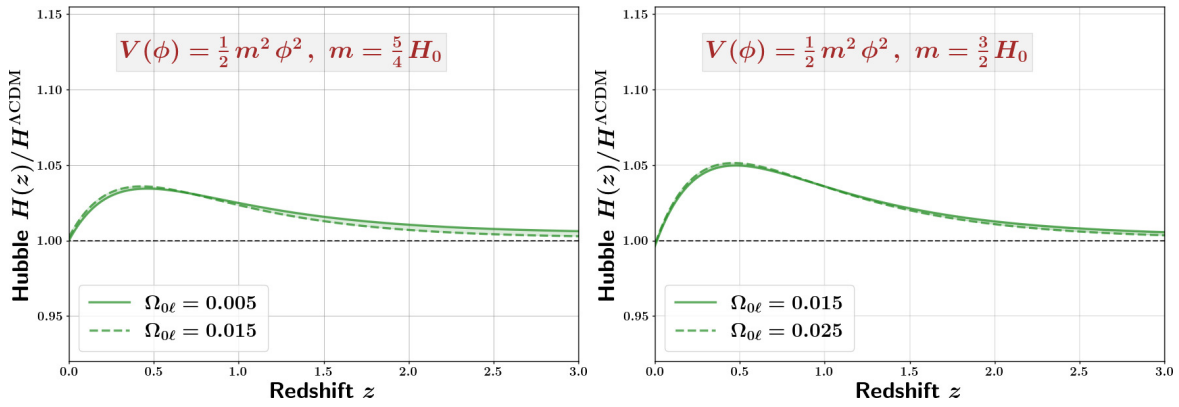

Figure 2. The Hubble parameter relative to ΛCDM is shown for the quadratic potential (3.1) with $m = \frac{5}{4} H_0$ (*left panel*), and $m = \frac{3}{2} H_0$ (*right panel*).

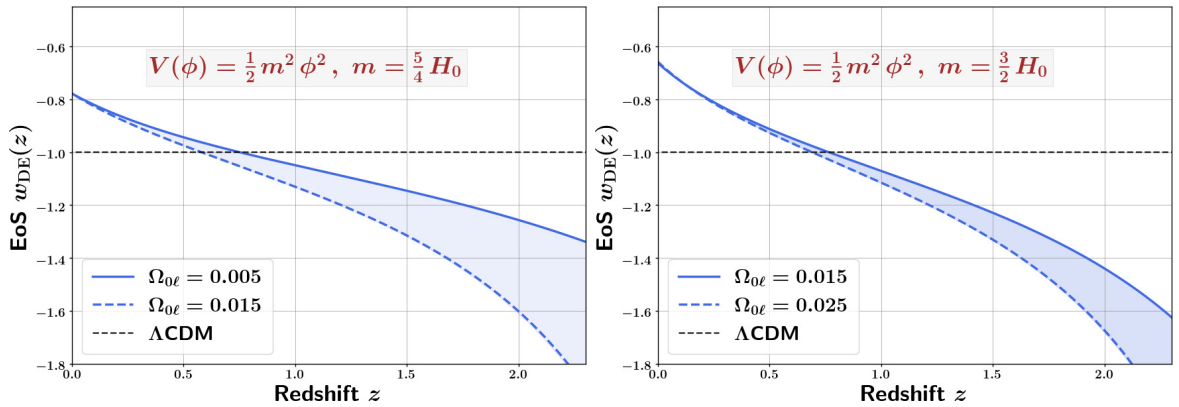

Figure 3. The DE equation-of-state parameter corresponding to the quadratic potential (3.1) is shown for $m = \frac{5}{4} H_0$ (*left panel*), and for $m = \frac{3}{2} H_0$ (*right panel*). Note that a larger value of the higher dimensional parameter, $\Omega_{0\ell}$, results in a lower redshift of phantom crossing.

The results of our simulations are illustrated in figures 2 and 3 for the evolution of the Hubble parameter (2.2) (relative to its value in ΛCDM) and the effective EoS of DE (2.11), respectively. Plots for the evolution of the density fraction of DE (2.10), the deceleration parameter (2.9) and the Om diagnostic (1.2) are shown in appendix B.1. Note that the plots are generated for two distinct values of the scalar field mass, namely, $m = \frac{5}{4} H_0$ and $\frac{3}{2} H_0$.

The blue curves in figure 3 demonstrate that the EoS of DE undergoes a phantom crossing in the recent past, leading to $w_{\text{DE}} > -1$ at the present epoch. For a fixed mass of the scalar field, comparing the solid and dashed blue curves in the left and right panels of figure 3, we notice that the epoch of phantom crossing gets shifted towards a lower redshift, while the DE EoS falls off sharply towards higher redshifts, upon increasing the value of $\Omega_{0\ell}$. In fact, this appears to be a universal feature of the braneworld parameter $\Omega_{0\ell}$ across all the potentials used in this work.

On the other hand, for a given $\Omega_{0\ell}$, an increase in the mass of the scalar field results in a steeper phantom crossing, and consequently, a higher DE EoS at the present epoch. However, if the mass is exceedingly high, i.e. $m/H_0 \gtrsim 1$, then the scalar field begins to oscillate prior

JCAP11(2025)018

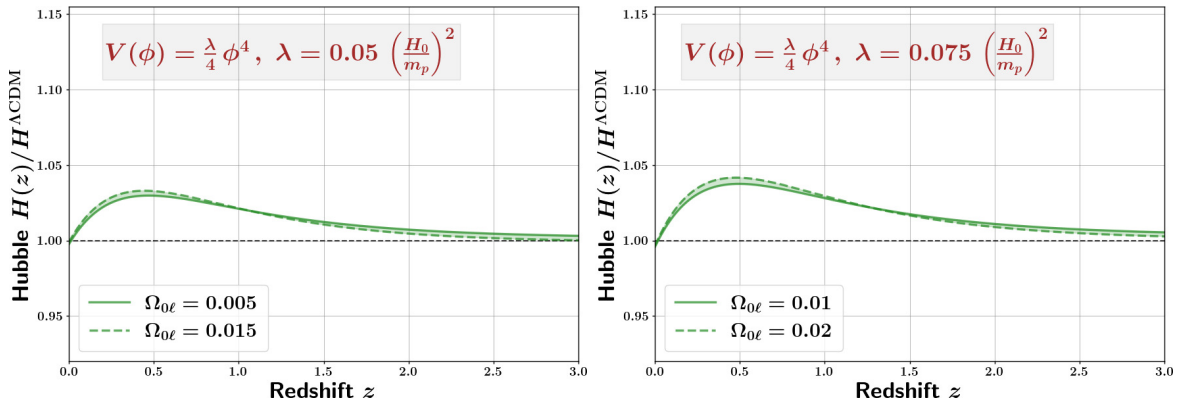

Figure 4. The Hubble parameter corresponding to the quartic potential (3.2) is shown for $\lambda = 0.05\,(H_0/m_p)^2$ (*left panel*), and $\lambda = 0.075\,(H_0/m_p)^2$ (*right panel*).

to the present epoch, leading to *phantom oscillations* [81], which is not consistent with the DESI DR2 results. Similarly, if the mass is very small, i.e. $m \ll H_0$, then the scalar field continues to remain frozen at its initial value, leading to $w_{\rm DE} \lesssim -1$ at the present epoch, with no phantom crossing.

A visual comparison of our plots in figure 2–3, with those of ref. [33], indicates that the DESI DR2 constraints appear to be consistent with a massive scalar field (on the brane) with parameters $m \sim H_0$, $\Omega_{0\ell} \sim 0.01$. As discussed before, for $\Omega_{0\ell} \to 0$, our model reduces to that of a scalar field with a quadratic potential in GR. A more systematic and detailed investigation of parameter estimation, involving MCMC analysis, is carried out in section 4, where results for the quadratic potential in GR ($\Omega_{0\ell} = 0$) is compared with that of the braneworld scenario ($\Omega_{0\ell} \neq 0$).

3.2 Quartic potential

We next turn our attention to the simple quartic potential, given by

$$V(\phi) = \frac{\lambda}{4}\,\phi^4\,. \tag{3.2}$$

The potential is schematically illustrated in the top-left panel of figure 1.

We perform numerical simulations for a range of (fixed) values of λ. The results of our simulations are illustrated in figure 4 and 5 for the evolution of the Hubble parameter (2.2) (relative to its value in ΛCDM) and the effective EoS of DE (2.11), respectively. Plots for the density fraction of DE (2.10), the deceleration parameter (2.9) and the Om diagnostic (1.2) are shown in appendix B.2. Note that these plots are generated for two distinct values of λ, namely, $\lambda = 0.05\,(H_0/m_p)^2$ and $\lambda = 0.075\,(H_0/m_p)^2$. For a given $\Omega_{0\ell}$, an increase in the value λ results in a steeper phantom crossing, and consequently, a higher DE EoS at the present epoch.

A visual comparison of our plots in figure 4–5, with those of ref. [33], indicates that DESI DR2 constraints appear to be well explained by the quartic potential on the phantom brane, closer to the range of parameters $\{\lambda,\, \Omega_{0\ell}\}$ used in these figures. A much larger or smaller value of λ will clearly not be compatible with the DESI constraints. A systematic parameter estimation for this model is carried out in section 4.

JCAP11(2025)018

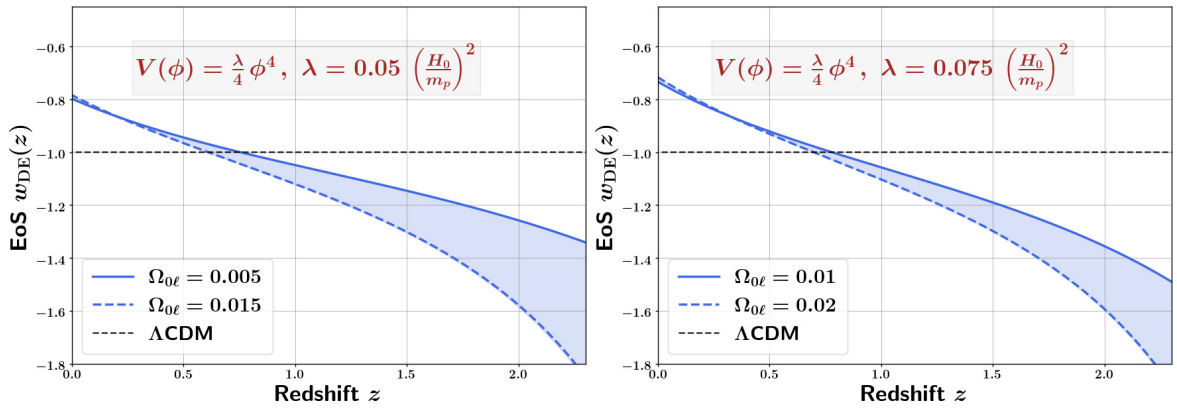

Figure 5. The DE EoS corresponding to the quartic potential (3.2) is shown for $\lambda = 0.05\,(H_0/m_p)^2$ (*left panel*), and for $\lambda = 0.075\,(H_0/m_p)^2$ (*right panel*). Note that a larger value of the higher dimensional parameter, $\Omega_{0\ell}$, results in a lower redshift of phantom crossing.

3.3 Symmetry-breaking potential

Consider the symmetry-breaking potential

$$V(\phi) = \frac{\lambda}{4}\left(\phi^2 - \nu^2\right)^2 , \tag{3.3}$$

where λ is the strength of self-interaction, while $\pm\nu$ is the vacuum expectation value of the field ϕ in the right and left vacua, respectively. The theory with this potential, schematically illustrated in the top-right panel of figure 1, is renormalisable and often appears in models of unification of gauge theories, including the Standard Model of particle physics.

Without loss of generality, we assume that the scalar field evolves on the right side, that is, $\phi > 0$. We then perform the field redefinition

$$\Phi = \phi - \nu\,. \tag{3.4}$$

The potential in terms of the new field takes the form

$$V(\Phi) = \frac{1}{2}\left(2\lambda\nu^2\right)\Phi^2 + \lambda\nu\,\Phi^3 + \frac{\lambda}{4}\,\Phi^4\,, \tag{3.5}$$

which indicates that the mass of the scalar field around the vacuum $\Phi = 0$ is given by

$$m_\Phi = \sqrt{2\lambda}\,\nu \quad \Rightarrow \quad \frac{m_\Phi}{H_0} = \sqrt{2\left(\frac{\lambda m_p^2}{H_0^2}\right)}\left(\frac{\nu}{m_p}\right) . \tag{3.6}$$

Given that there are two free parameters in the potential, namely, $\{\lambda, \nu\}$, we carry out the simulations systematically for different (fixed) values of the mass parameter m_Φ. Eq. (3.6) then relates ν with a given choice of λ. Around this right-side vacuum, the scalar field can begin its descent from its frozen state either along the steep right wing or the flat hilltop of the potential (as illustrated by the brown circles and arrows in the top-right panel of figure 1), depending on the initial conditions in the early universe.

To facilitate comparison between our results for the symmetry-breaking potential and those for the quadratic and quartic potentials, we explicitly generate the plots using the values of m_Φ and λ which give results similar to those in section 3.1 and section 3.2, respectively.

JCAP11(2025)018

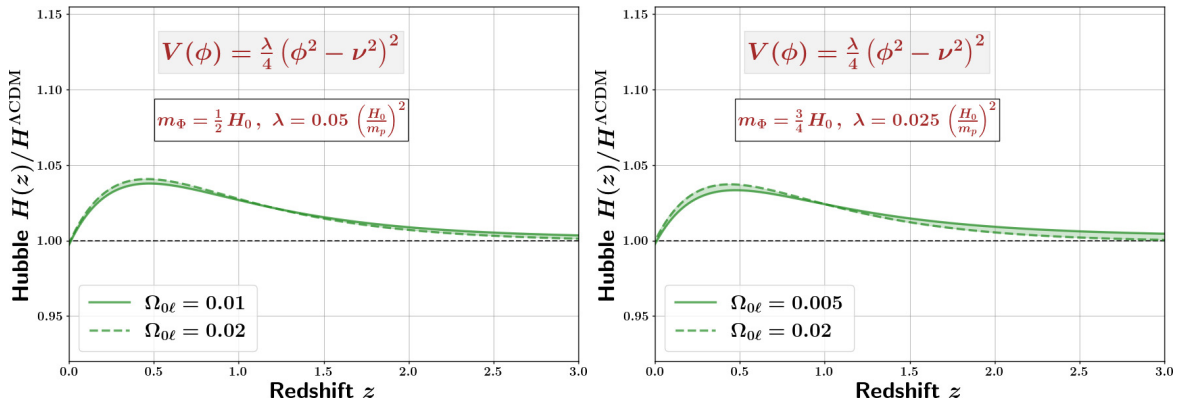

Figure 6. The Hubble parameter corresponding to the steep right wing of the symmetry-breaking potential (3.3) is shown for $m_\Phi = \frac{1}{2} H_0\,,\ \lambda = 0.05\,(H_0/m_p)^2$ (*left panel*), and $m_\Phi = \frac{3}{4} H_0\,,\ \lambda = 0.025\,(H_0/m_p)^2$ (*right panel*).

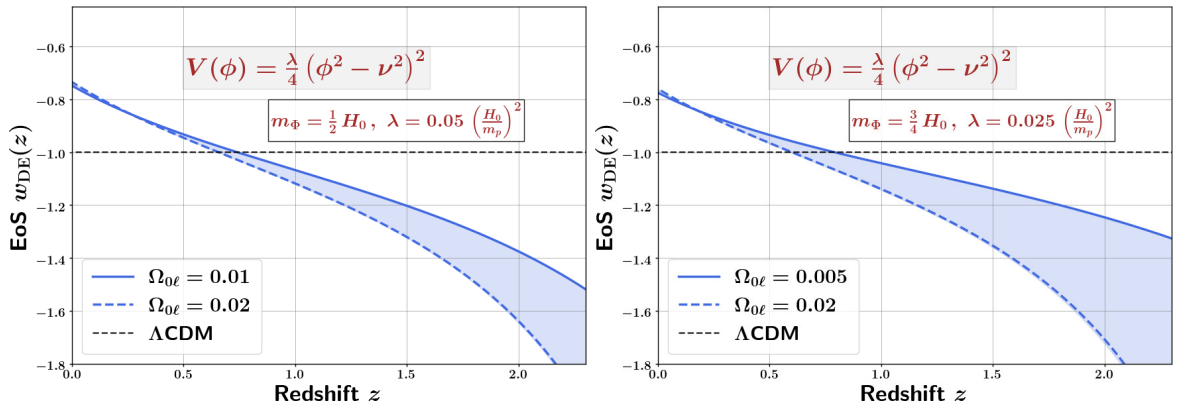

Figure 7. The DE equation-of-state parameter corresponding to the steep right wing of the symmetry-breaking potential (3.3) are shown for $m_\Phi = \frac{1}{2} H_0\,,\ \lambda = 0.05\,(H_0/m_p)^2$ (*left panel*), and for $m_\Phi = \frac{3}{4} H_0\,,\ \lambda = 0.025\,(H_0/m_p)^2$ (*right panel*). Note that a larger value of the higher dimensional parameter, $\Omega_{0\ell}$, results in a lower redshift of phantom crossing.

3.3.1 Descent from the steep wing

Our results for parameter values $\{m_\Phi,\, \lambda\}$ relevant for scalar-field evolution along the steep right wing are illustrated in figure 6 and 7 for the evolution of the Hubble parameter (2.2) (relative to its value in ΛCDM) and the effective EoS of DE (2.11), respectively. Plots for the density fraction of DE (2.10), the deceleration parameter (2.9) and the Om diagnostic (1.2) are shown in appendix B.3.

A visual comparison of our plots with those of ref. [33] indicates that the DESI constraints can be accommodated by the steep right wing of the symmetry-breaking potential on the phantom brane, provided that both m_Φ and λ are close to the values in our plots. When these parameters are exceedingly large, the effective dynamical dark energy undergoes a phantom crossing that occurs too early and too abruptly, which is inconsistent with the DESI DR2 constraints. For a more robust and systematic estimation of the parameters, see section 4.

JCAP11(2025)018

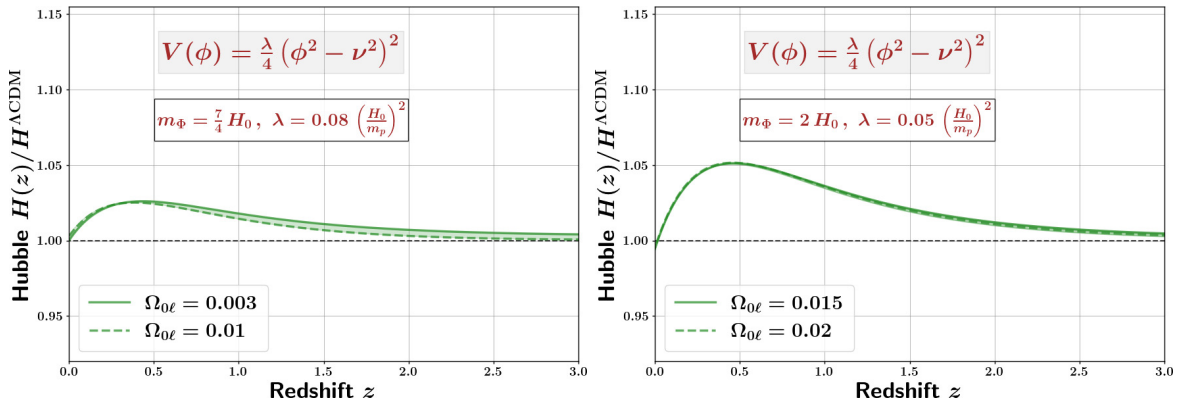

Figure 8. The Hubble parameter corresponding to the flat left wing of the symmetry-breaking potential (3.3) is shown for $m_\Phi = \frac{7}{4} H_0\,,\ \lambda = 0.08\,(H_0/m_p)^2$ (*left panel*), and $m_\Phi = 2\,H_0\,,\ \lambda = 0.05\,(H_0/m_p)^2$ (*right panel*).

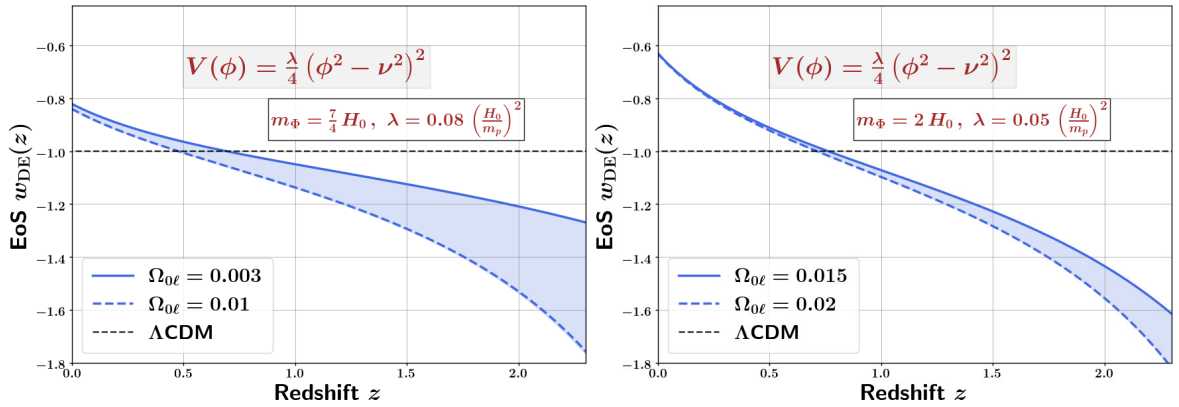

Figure 9. The DE equation-of-state parameter corresponding to the flat left wing of the symmetry-breaking potential (3.3) is shown for $m_\Phi = \frac{7}{4} H_0\,,\ \lambda = 0.08\,(H_0/m_p)^2$ (*left panel*), and for $m_\Phi = 2\,H_0\,,\ \lambda = 0.05\,(H_0/m_p)^2$ (*right panel*). Note that a larger value of the higher dimensional parameter, $\Omega_{0\ell}$, results in a lower redshift of phantom crossing.

3.3.2 Descent from the flat wing

Our results for a range of parameter values of $\{m_\Phi,\, \lambda\}$ relevant for scalar-field evolution along the flat left wing are illustrated in figure 8 and 9 for the evolution of the Hubble parameter (2.2) (relative to its ΛCDM value) and the effective EoS of DE (2.11) respectively. Plots for the density fraction of DE (2.10), the deceleration parameter (2.9) and the Om diagnostic (1.2) are shown in appendix B.4. A rudimentary comparison of our plots with those of ref. [33] indicates that the DESI constraints are reasonably well explained by the flat left wing of the symmetry-breaking potential on the phantom brane, provided that both m_Φ and λ are relatively higher than those in the case of the steep right wing discussed in section 3.3.1, as can be seen by comparing figure 9 with figure 7.

We note that for a given value of the effective mass (m_Φ), a flatter potential is relatively less effective in explaining the DESI DR2 constraints compared to a quadratic potential of the same mass, as discussed in section 4.3. This is due to the fact that flat potentials

JCAP11(2025)018

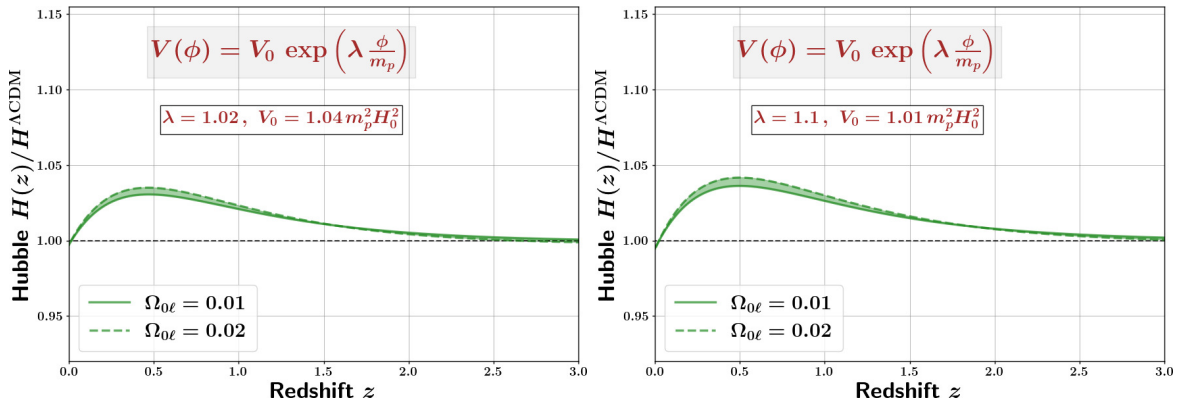

Figure 10. The Hubble parameter corresponding to the exponential potential (3.7) is shown for $\lambda = 1.02$, $V_0 = 1.04\, m_p^2 H_0^2$ (*left panel*), and for $\lambda = 1.1$, $V_0 = 1.01\, m_p^2 H_0^2$ (*right panel*).

display shallower rate of phantom crossing as compared to steeper potentials. Therefore, they require relatively larger values of the effective mass in order to be consistent with the data. A systematic estimation of parameters is carried out in section 4 using MCMC.

3.4 Exponential potential

The exponential potential

$$V(\phi) = V_0 \exp\left(\lambda \frac{\phi}{m_p}\right), \tag{3.7}$$

is ubiquitous in both early-Universe [82, 83] and late-Universe [84, 85] cosmology, and appears naturally in string theory [86–88]. In standard GR, a pure exponential potential with $\lambda < \sqrt{2}$ behaves like DE, while $\lambda > \sqrt{2}$ does not result in late-time acceleration.[9] However, in the braneworld scenario, it is possible to obtain transient late-time acceleration from exponential potentials[10] with $\lambda \gtrsim \sqrt{2}$.

Our results for a range of parameter values of λ, V_0 of the exponential potential are illustrated in figure 10 and 11 for the evolution of the Hubble parameter (2.2) (relative to its ΛCDM value) and the effective EoS of DE (2.11) respectively. Plots for the density fraction of DE (2.10), the deceleration parameter (2.9) and the Om diagnostic (1.2) are shown in appendix B.5.

A visual comparison of our plots with those of ref. [33] indicates that the DESI DR2 constraints can be accommodated by the exponential potential for $\lambda \approx \mathcal{O}(1)$. However, a more systematic parameter estimation using MCMC is discussed in section 4.

[9] In particular, an exponential potential with $\lambda^2 > 3(1 + w_B)$ in a Universe dominated by a perfect fluid with EoS w_B results in a scaling attractor solution [84]. Therefore, modifications to the exponential potential is desired [89–93] in order to realise DE in GR. In fact, our analysis of DE in the braneworld for the pure exponential potential will also carry over conveniently to modifications of the exponential function, such as $V(\phi) = V_0\ [\cosh(\lambda\phi/m_p) - 1]$ [91].

[10] In GR, a scalar field with steep exponential potential ($\lambda \gtrsim \sqrt{2}$) with a matter-coupling has been studied in ref. [59] in the context of DESI DR2.

JCAP11(2025)018

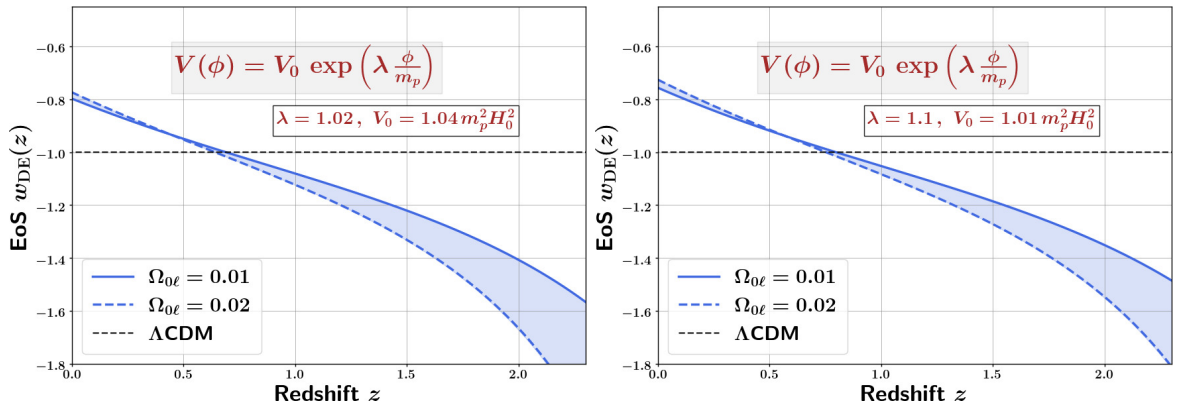

Figure 11. The DE equation-of-state parameter corresponding to the exponential potential (3.7) is shown for $\lambda = 1.02$, $V_0 = 1.04\, m_p^2 H_0^2$ (*left panel*), and for $\lambda = 1.1$, $V_0 = 1.01\, m_p^2 H_0^2$ (*right panel*). Note that a larger value of the higher dimensional parameter, $\Omega_{0\ell}$, results in a lower redshift of phantom crossing.

3.5 Axion potential

The potential for a (pseudo) Nambu-Goldstone boson of the axion type is given by

$$V(\phi) = V_0 \left[1 - \cos\left(\frac{\phi}{\mathcal{F}}\right)\right] , \tag{3.8}$$

where $\mathcal{F}$ is the axion decay constant. The potential is schematically illustrated in the bottom-left panel of figure 1 by purple curves, corresponding to a fixed value of V_0 and different values of $\mathcal{F}$.

Note that, for $\phi \ll \mathcal{F}$, the potential can be approximated as a quadratic up to leading order in $\phi/\mathcal{F}$, that is,

$$V(\phi)\big|_{\phi \ll \mathcal{F}} \simeq \frac{1}{2} m_{\mathcal{A}}^2 \phi^2 - \mathcal{O}\left(\frac{\phi}{\mathcal{F}}\right)^4 , \tag{3.9}$$

with

$$m_{\mathcal{A}}^2 = \frac{V_0}{\mathcal{F}^2} , \tag{3.10}$$

which is illustrated by gray-colour plots in the bottom-left panel of figure 1.

Our results for a range of parameter values of $\{m_{\mathcal{A}}, \mathcal{F}\}$ for the Axion potential are illustrated in figure 12 and 13 for the evolution of the Hubble parameter (2.2) (relative to its ΛCDM value) and the effective EoS of DE (2.11) respectively. Plots for the density fraction of DE (2.10), the deceleration parameter (2.9) and the Om diagnostic (1.2) are shown in appendix B.6.

A visual comparison of our plots with those of ref. [33] indicates that the DESI DR2 constraints can be accommodated by the Axion potential, provided $m_{\mathcal{A}}$ is somewhat larger than in the case of the quadratic potential discussed in section 3.1.

This is due to the fact that a flat potential, such as the Axion potential (3.8) which is bounded from above (and of course, from below), is always less steep than a quadratic potential of the same effective mass. In fact, for a given mass $m_{\mathcal{A}}$, choosing a large $\mathcal{F}$

JCAP11(2025)018

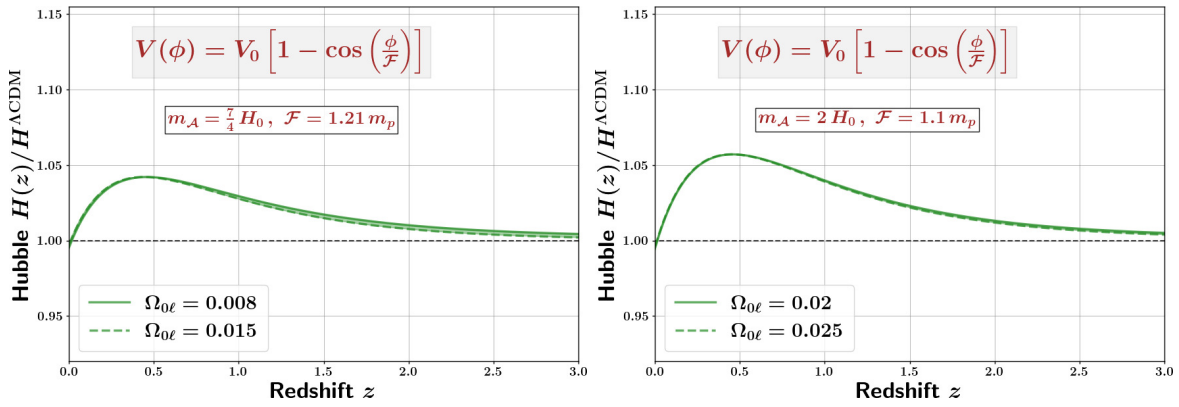

Figure 12. The Hubble parameter corresponding to the Axion potential (3.8) is shown for $m_{\mathcal{A}} = \frac{7}{4} H_0$, $\mathcal{F} = 1.21\, m_p$ (*left panel*), and $m_{\mathcal{A}} = 2\, H_0$, $\mathcal{F} = 1.1\, m_p$ (*right panel*).

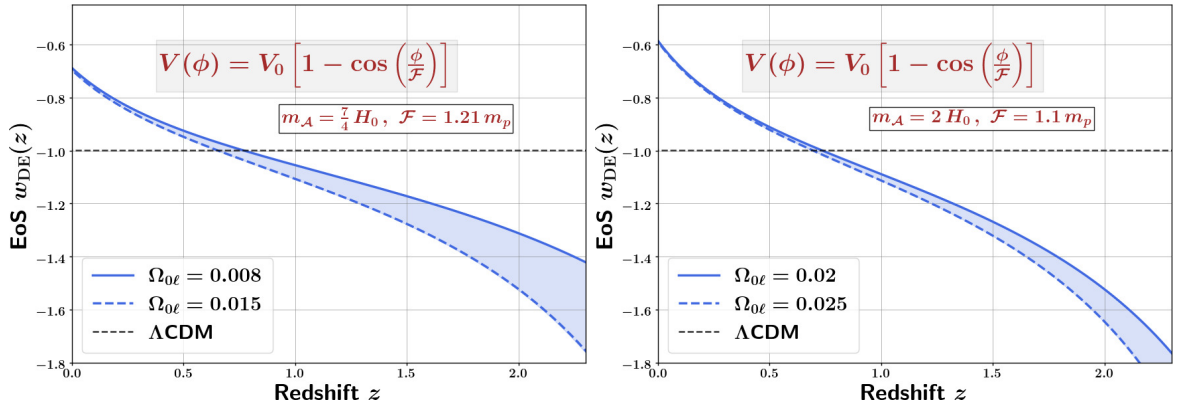

Figure 13. The DE equation-of-state parameter corresponding to the Axion potential (3.8) is shown for $m_{\mathcal{A}} = \frac{7}{4} H_0$, $\mathcal{F} = 1.21\, m_p$ (*left panel*), and for $m_{\mathcal{A}} = 2\, H_0$, $\mathcal{F} = 1.1\, m_p$ (*right panel*). Note that a larger value of the higher dimensional parameter, $\Omega_{0\ell}$, results in a lower redshift of phantom crossing.

corresponds to maximal steepness. In this limit, its behaviour mimics that of the quadratic potential, discussed in section 3.1. However, in the opposite limit, where $\mathcal{F}$ is as small as possible, the potential is much flatter. Phantom crossing occurs more slowly and it is less effective in describing the DESI DR2 data. Our plots in figures 12–13, are generated for rather intermediate values of $\mathcal{F}$, namely, $\mathcal{F} = 1.1$, and 1.21. A more systematic parameter estimation using MCMC is discussed in section 4.

4 Observational constraints from DESI DR2

4.1 Data combination

In order to further gauge the viability of the models in the context of observed data, we perform a Markov Chain Monte Carlo (MCMC) analysis using a combination of the following most recent cosmological datasets:

Type Ia Supernovae (SNe Ia): we make use of the Union 3 compilation [94], which is based on a collection of 2087 Type Ia supernovae in the redshift range $0.05 < z < 2.26$.

JCAP11(2025)018

The data comprise 22 distance modulus values, determined through the implementation of the Unity 1.5 Bayesian hierarchical framework, which allows for constraint of the expansion history through the luminosity distance $D_L(z)$. In our analysis we marginalize over the B-band absolute magnitude, M_B. Though there are differences between the methodology and results from the three latest supernovae compilations (Union-3, Pantheon+ [95] and DES 5-year [96]), they have been shown to display a degree of consistency such that we do not expect our results to change if we were to use one of the other ones instead [97]. Here we select Union-3 because of the relative computational ease that arises by virtue of the smaller associated covariance matrix.

Baryon Acoustic Oscillations (BAO): using the DESI DR2 [98], we gain access to further constraints on the expansion history through the Hubble distance $D_H(z)$, the angular diameter distance $D_M(z)$ and the angle-averaged distance $D_V(z)$. The first two kinds of distance measurements are collected in six redshifts in the range $0.51 < z < 2.33$, while the angle-averaged measurement has an effective redshift of $z = 0.295$.

CMB (compressed): in order to ensure the viable high-redshift behaviour of the resulting model fits, we make use of a combination of *Planck* and Atacama Cosmology Telescope (ACT) CMB data. In particular, for reasons of numerical efficacy,[11] we use CMB distance priors R, ℓ_a, ω_b, first used for this purpose by [99], and shown to be a robust compression of CMB data. Since these require high redshift quantities to be computed, the differential equations are solved starting at much higher redshift ($z > 1000$) in the MCMC than in the analysis presented so far. The data and covariance of the CMB distance priors are taken from [100] where they are computed for the PR3 *Planck* PLIK likelihood [101] and the Data Release 6 of the Atacama Cosmology Telescope [102].

4.2 MCMC results

We make use of the publicly available likelihoods along with custom theory code implemented in `Cobaya` [103] to perform the parameter estimation, using MCMC sampling. The best-fit parameter values for the various models are reported in table 1, and compared with the results for the CPL parametrisation [12] under the same framework. What is striking is that the χ^2 values of all of the models are very close to that of the CPL parametrisation (i.e. $|\Delta\chi^2| \ll 1$), indicating that the fits to the actual data of the models we investigate are able to attain a level comparable with CPL.

In fact, the median $w_{\rm DE}(z)$ curves of all our braneworld DE models display phantom behaviour for redshifts $z \gtrsim 0.5$, before crossing the phantom divide line at lower redshifts to exhibit $w_{\rm DE}(z) > -1$ at the present epoch, as can be seen in figure 14. It is also interesting to note that the low-redshift behaviour of the EoS of DE in all our models differs from that of the CPL parametrisation in a similar way, which is discussed in more detail in section 4.3.

[11] Using the full CMB likelihood would require careful and lengthy modifications to the dynamics of cosmological perturbations inside a Boltzmann solver, which we reserve for a future work.

[12] Although we display the best-fit curves and contours for the CPL parametrisation here, it is important to stress the fact that the phantom-crossing preference of the DESI DR2 dataset is not merely a consequence of CPL parametrisation. Rather, a wide variety of reconstructions of the DE EoS prefer the phantom-crossing behaviour [33, 104–106].

JCAP11(2025)018

Parameters ⟶ Models ↓	Ω_{0m}	H_0 (km/s/Mpc)	$\Omega_{0b}h^2$	Model Par-I	Model Par-II	$\Omega_{0\ell}$ ($\pm 68\%$)	$\Delta\chi^2$ ($\equiv \chi^2 - \chi^2_{\rm CPL}$)
CPL	0.3276	66.13	0.02238	$w_0 = -0.67$	$w_a = -1.07$	—	0
Quadratic (GR)	0.3209	66.32	0.02254	$\frac{m}{H_0} = 1.038$	—	—	7.99
Quadratic	0.3239	66.53	0.02236	$\frac{m}{H_0} = 1.26$	—	$0.0132^{+0.0098}_{-0.0082}$	0.06
Quartic	0.3241	66.52	0.02239	$\frac{\lambda m_p^2}{H_0^2} = 0.0514$	—	$0.0136^{+0.0125}_{-0.0049}$	0.19
SB Steep	0.3241	66.48	0.02238	$\frac{m_\Phi}{H_0} = 1.17$	$\mathbf{\frac{\lambda m_p^2}{H_0^2} = 0.0012}$	$0.0127^{+0.01216}_{-0.0057}$	0.09
SB Flat	0.3252	66.41	0.02237	$\frac{m_\Phi}{H_0} = 2.68$	$\mathbf{\frac{\lambda m_p^2}{H_0^2} = 0.64}$	$0.0115^{+0.0081}_{-0.005}$	-0.16
Axion	0.3243	66.48	0.02238	$\frac{m_A}{H_0} = 1.28$	$\mathbf{\frac{\mathcal{F}}{m_p} = 6.40}$	$0.01302^{+0.0087}_{-0.0076}$	0.06
Exp	0.3227	66.65	0.02237	$\lambda = 0.997$	$\mathbf{\frac{V_0}{m_p^2 H_0^2} = 0.846}$	$0.0142^{+0.0064}_{-0.0084}$	0.24

Table 1. Best-fit values of different parameters corresponding to the medians of the MCMC chains for various potentials are tabulated here. Very small values of $\Delta\chi^2$ (except for the GR case) in the bottom-most row indicate that our models explain the latest observational results (combining DESI DR2, Union 3 and CMB *Planck* + ACT datasets) very well, at least as well as the CPL parametrisation.

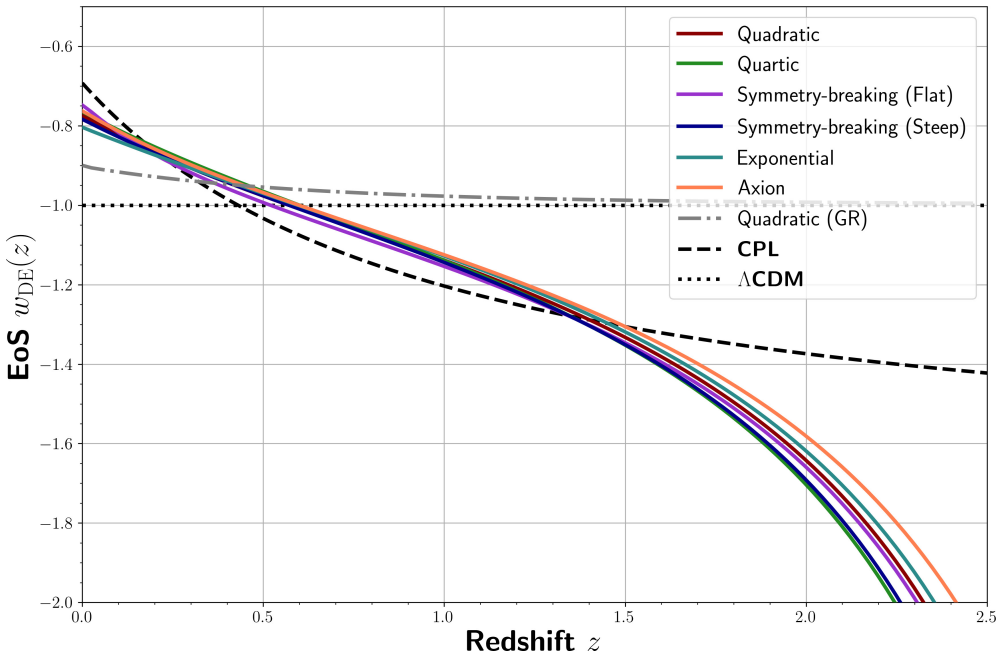

Figure 14. Best-fit curves of the effective EoS of DE, $w_{\rm DE}(z)$, corresponding to the medians of the MCMC chains are shown in coloured solid curves, for various potentials considered in this work: quadratic potential (red), quartic potential (green), steep wing (blue) and flat wing (purple) of the symmetry-breaking potential, the exponential potential (cyan) and the Axion potential (orange). The corresponding curve for the CPL parametrisation is shown as a dashed black curve. EoS for the quadratic potential in GR is shown in dot-dashed gray curve. Similarly, the constant EoS of DE in ΛCDM, namely, $w_{\rm DE} = -1$, is shown as a dotted black (horizontal) line.

JCAP11(2025)018

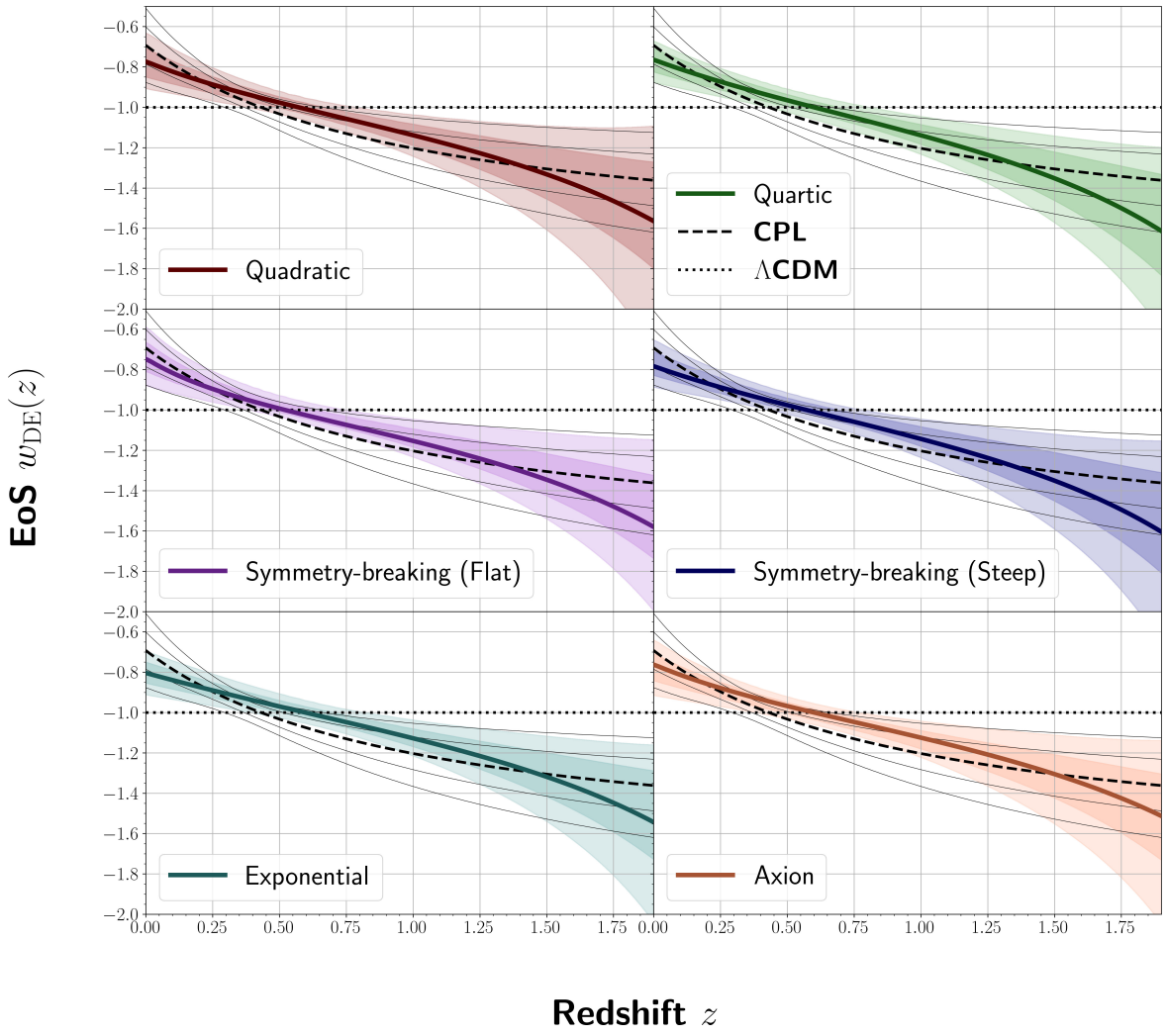

Figure 15. 1σ and 2σ contours for the effective EoS $w_{\rm DE}(z)$ of DE for various potentials considered in this work are shown, along with the CPL contours. The medians of the samples from each model are shown in coloured solid curves, while the CPL EoS is shown as a dashed black curve, with finer solid black contours. The ΛCDM expectation of a constant DE EoS at $w_{\rm DE}(z) = -1$ is shown with a dotted horizontal black line.

In figures 15 and 16 we show the median curves of $w_{\rm DE}(z)$ and $H(z)/H^{\Lambda\rm CDM}(z)$, for each potential considered in this work, along with the 1σ and 2σ contours calculated from the MCMC samples. For comparison, we plot also the corresponding curve and contours for the CPL parametrisation, demonstrating that the general dynamics of dark energy in the braneworld displays a behaviour similar to that of CPL parametrisation,[13] when constrained using the latest cosmological datasets.

These results suggest that the physical models investigated here serve as viable explanations for the observed data, at least at the level of the CPL parametrisation and within the precision achieved using the current datasets. More importantly, the phantom divide

[13]However, see section 4.3 for a discussion on comparison between different potentials in the braneworld scenario considered in this work, as well as contrasting them with the CPL parametrisation.

JCAP11(2025)018

crossing behaviour, which is suggested by the CPL parametrisation (as well as non-parametric methods, see refs. [33, 105]) is explained physically, within the framework of thawing scalar field potentials in the braneworld scenario.

It is worth noting that in GR ($\Omega_{0\ell} = 0$), the DE EoS for these scalar field potentials does not exhibit phantom-divide crossing, as explicitly shown for the quadratic potential in the dot-dashed gray curve of figure 14. In GR, the quadratic potential yields a significantly larger value of χ^2 relative to CPL, with $\Delta\chi^2 \equiv \chi^2 - \chi^2_{\rm CPL} \simeq 7.99$, indicating a poor fit to the datasets. We find that this behaviour persists for all other potentials considered in this work. Moreover, $\Omega_{0\ell} = 0$ lies well outside the 1–2 σ bounds on the best-fit values of $\Omega_{0\ell}$, as shown in figure 17 (the 1 σ bounds on $\Omega_{0\ell}$ are explicitly listed in table 1). Therefore, we conclude that scalar field DE in pure GR provides a poor fit to the data, whereas the braneworld scalar field models with $\Omega_{0\ell} \neq 0$ deliver a statistically significant improvement, offering a physically compelling realization of dynamical dark energy in light of the latest observations.

Before moving forward, it is worth highlighting that for potentials with a single parameter, such as the quadratic and quartic potentials (along with the brane parameter $\Omega_{0\ell}$), all the parameters quoted in table 1 are well constrained by the data. However, for two-parameter potentials, such as the symmetry-breaking, exponential and Axion potentials, the second parameter for each potential (marked in bold numbers) is not very well constrained by the data. Hence, there appears to be a degeneracy that the considered datasets are unable to break, as can be seen more clearly from the bottom-most row of each panel of the triangle plots in figure 17. The best-fit values of these parameters, as quoted in table 1, should therefore be taken not-too-literally. In fact, a range of values of the second parameter of each of these three potentials yields χ^2 values that are comparable to each other.

4.3 Comparison of results for different potentials

In the preceding analysis, the quadratic (3.1) and quartic (3.2) potentials in the braneworld scenario (with $\Omega_{0\ell}$) belong to two-parameter class of models, similar to the CPL parametrisation, while the symmetry-breaking (3.3.1), exponential (3.7) and axion (3.8) potentials are three-parameter models. By comparing our results in figures 2–3 for the quadratic potential with figures 4–5 for the quartic potential, we observe that both potentials perform almost equally well — based purely on visual inspection (this can also be inferred more quantitatively from the values of $\Delta\chi^2$ displayed in table 1). This is somewhat surprising, as one might expect that the quartic potential would perform better due to its ability to produce a sharper phantom crossing. Similarly, the results for the steep wing of the symmetry breaking potential in figures 6–7 are similar to those of the flat wing of the symmetry breaking potential in figures 8–9, as well as to those of the Axion potential in figures 12–13.

The reason for this similarity lies in the fact that the slopes of these potentials — within the range of field values relevant to the system's full evolution (from $z = 99$ to $z \lesssim -1$, as used in our simulations) — are of the same order of magnitude for the chosen parameter values in the figures. This is illustrated clearly in figure 18, which directly compares these potentials.

However, it is important to stress that for a given (effective) mass, flat potentials, such as the Axion potential (3.8) and the flat wing of the symmetry-breaking potential (3.3), are always less steep compared a quadratic potential (3.1) of the same mass. Since DESI DR2

JCAP11(2025)018

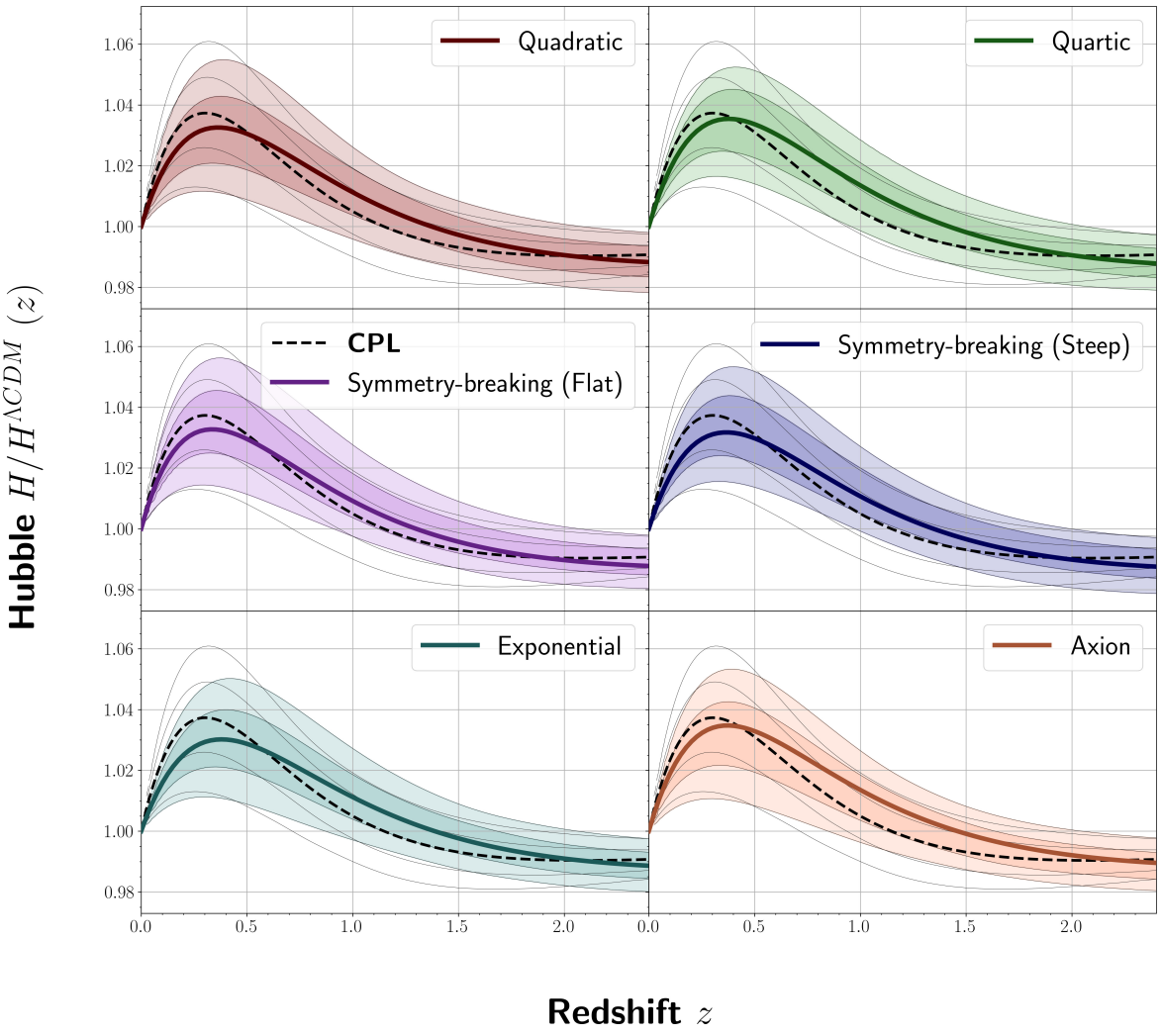

Figure 16. 1σ and 2σ contours for the ratio of the Hubble factor to its ΛCDM counterpart are shown for each potential considered in this work. The medians of the samples from each model are shown in coloured solid curves. The corresponding median and contours for the CPL parametrisation are shown as dashed black curve and fine solid black curves, respectively.

prefers a relatively steeper change in the DE EoS around the phantom crossing, the flat potentials can explain the observed results for relatively higher values of the (effective) mass as compared to the quadratic potential, as observed in our simulations, also see table 1.

There are a number of important points to highlight here in order to contrast between the DE dynamics for the CPL parametrisation and the potentials considered in our braneworld scenario, such as,

1. At relatively higher redshifts (towards the right-hand side of figure 14), the EoS of DE for the CPL parametrisation is different from our models. This is because the EoS in our models approach a pole in $w(z)$ as discussed in appendix A. Therefore, our models exhibit concave-shaped EoS curves, as opposed to the CPL curves which are necessarily convex, as can be inferred from eq. (1.1).

JCAP11(2025)018

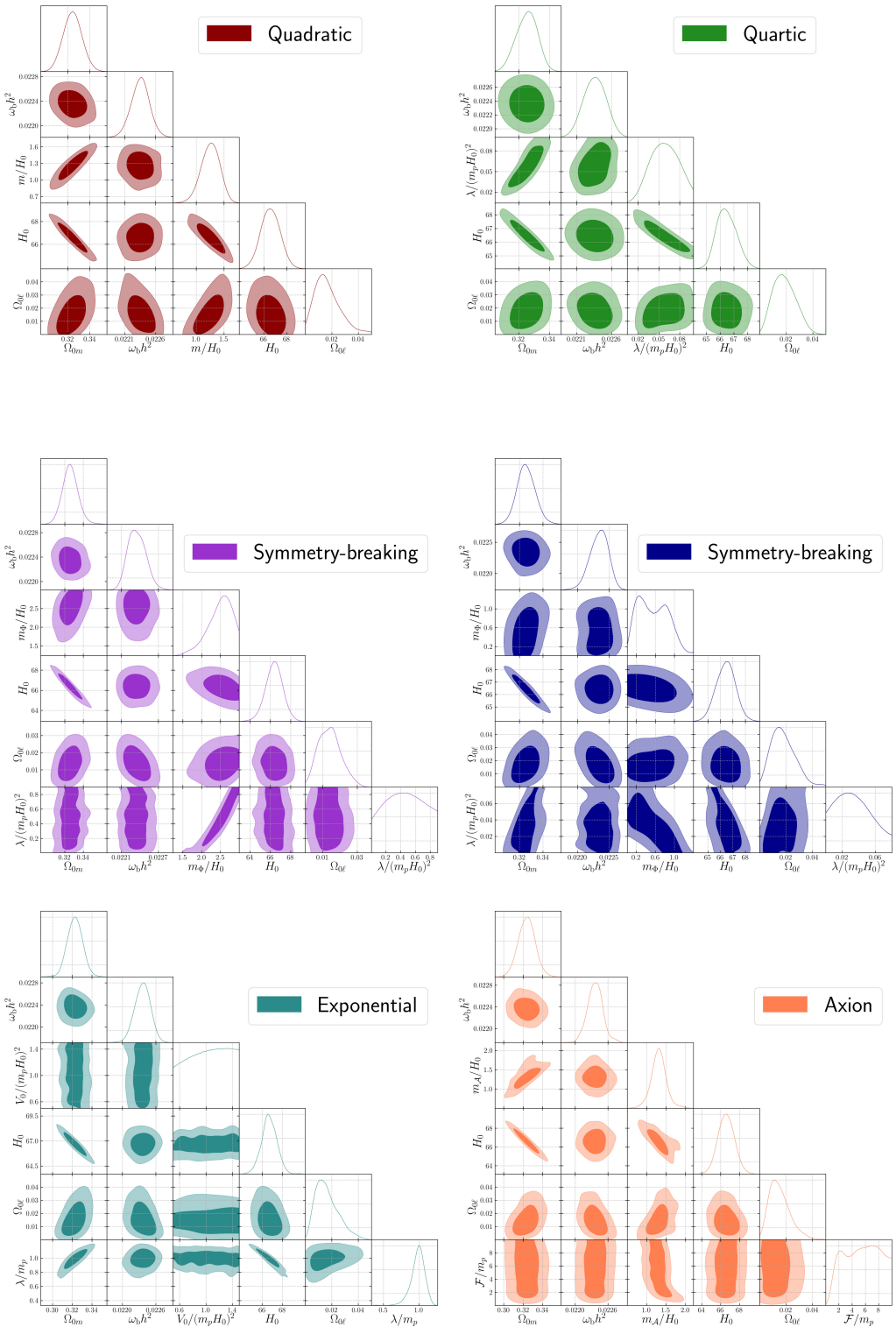

Figure 17. A triangle plot displaying the posterior distribution of observables listed in table 1 for various potentials considered in this work, namely, the quadratic potential in the *top-left panel*, the quartic potential in the *top-right panel*, the symmetry breaking potential with flat wing in the *middle-left panel* and with steep wing in the *middle-right panel*, and finally the exponential potential in the *bottom-left panel* and the axion potential in the *bottom-right panel*.

JCAP11(2025)018

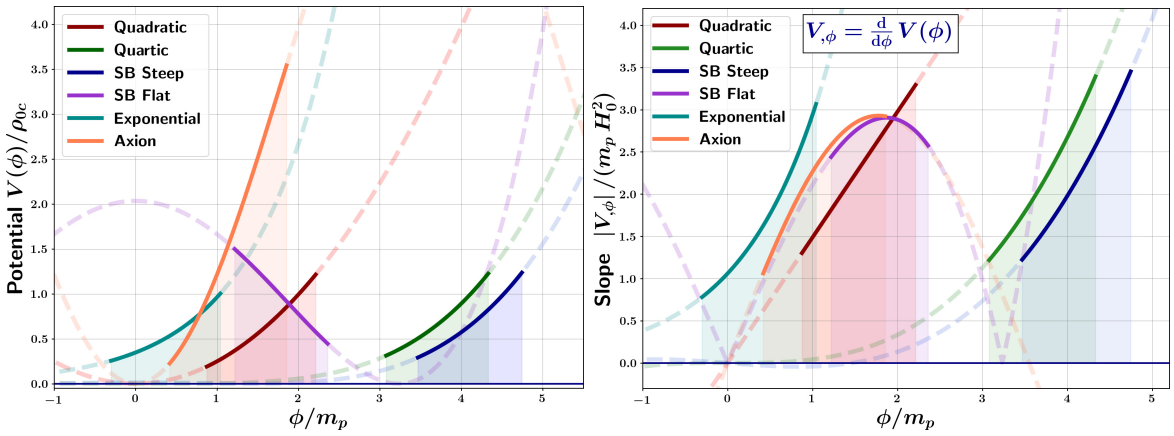

Figure 18. *Left panel* shows the quadratic potential (red), quartic potential (green), steep wing (blue) and flat wing (purple) of the symmetry-breaking potential, the exponential potential (teal) and the Axion potential (orange); while the *right panel* shows the corresponding slopes of these potentials. The *darker (solid) curves* with vertical shades correspond to the field (ϕ) range explored during the full simulation time, i.e. from $z = 99$ to $z \lesssim -1$. The *fainter (dashed) curves* correspond to plots of $V(\phi)$ and $V_{,\phi}$ for much larger range of ϕ values. We have plotted each potential and its derivative for parameters which correspond to $\Delta\chi^2$ values that are very close to the $\Delta\chi^2$ values quoted in table 1 for the best-fit parameters.

Of course, at very high redshifts, $z \gg 1$, the CPL EoS tends towards a constant, given by (from best-fit values in the table)

$$w_{\mathrm{DE,\,CPL}} \to w_0 + w_a \simeq -1.74\,, \quad z \gg 1\,,$$

and so do our EoS curves, which tend towards $w_{\mathrm{DE}} \to -0.5$ deep inside the matter domination, because the deceleration parameter $q(z) \to 0.5$.

2. At lower redshifts, $z \ll 1$, eq. (1.1) demonstrates that the CPL EoS changes linearly with redshift displaying a constant slope, namely,

$$w_{\mathrm{DE,\,CPL}} = w_0 + w_a \times z \simeq -0.67 - 1.07 \times z\,, \quad z \ll 1\,.$$

For the thawing potentials in our braneworld scenario, the behaviour is more complicated and depends on the slope of the potential used. However, in our thawing DE models, since the potential is decreasing as we approach $z = 0$, the scalar field is closer to its minimum and ρ_ϕ is much smaller than its frozen value at higher redshifts. Hence, the value of the EoS is primarily dictated by $\Omega_{0\ell}$, see eq. (13) in ref. [76]. The best-fit values of $\Omega_{0\ell}$ (given DESI DR2) for all our models are therefore almost equal, and hence the EoS of DE in all these model behaves similarly around $z \simeq 0$. Small differences come from the fact that closer to $z = 0$, $V(\phi)$ and $V_{,\phi}$ for these models are slightly different, as can be seen from figure 18.

For a choice of model parameters sufficiently far away from the best-fit values quoted in table 1, the scalar field might remain frozen until the present epoch. In that case it will behave like a cosmological constant (on the brane) and the present EoS of DE will

JCAP11(2025)018

be phantom-like with $w_{\rm eff} < -1$. For such a choice of parameter space, the EoS of DE will not exhibit phantom-crossing by $z = 0$.

5 Discussion

The recent DESI observations regarding the evolution of cosmic dark energy — particularly the indication of a phantom crossing — are both surprising and difficult to reconcile within the framework of standard single-component dynamical dark energy models. If interpreted literally, these results suggest a more complex underlying physics than previously anticipated.

To address this challenge and replicate the dark energy behaviour established by DESI, we explore a new cosmological model consisting of a scalar field propagating on the ghost-free braneworld with a single extra spatial dimension. Both scalar field and braneworld may arise quite naturally from a more fundamental superstring or higher-dimensional theoretical framework. In this framework, the scalar field serves as the only source of thawing dark/vacuum energy on the brane. Braneworld DE on its normal (ghost-free) branch is known to exhibit universal phantom-like features [45, 48] which we utilise to model early-time evolution. At early times, an ultra-light scalar field remains frozen to its initial value resulting in an effective phantom-like EOS of dark energy with $w_{\rm DE} < -1$ at $z \geq 1$. As the universe expands, the dynamics of the scalar field becomes increasingly prominent, introducing quintessential characteristics at later times. This interplay naturally leads to a crossing of the phantom divide within our models so that the EoS of DE exhibits $w_{\rm DE} > -1$ at $z \lesssim 1$.

We find that scalar fields with a variety of thawing potentials are quite effective in realizing this behaviour. Notably, simple potentials — such as quadratic, quartic, symmetry-breaking, exponential and axion — yield excellent results, and offer a compelling quantitative fit to the DESI DR2 data when analysed using MCMC sampling. In fact, single-parameter potentials, such as the quadratic or quartic potential, are able to explain the observational data as well as the frequently employed CPL parametrisation. Our models therefore represent a physically well-motivated scenario for explaining the latest observational results from DESI.

It will be interesting to extend the present analysis, which has been carried out at the level of background cosmological dynamics, by investigating the evolution of linear perturbations in the braneworld scenario [107] in the presence of the scalar field. Such an analysis would provide a more comprehensive understanding of the model's viability, particularly in the context of structure formation and the growth history of cosmic inhomogeneities. Previous studies have shown that the growth of perturbations in braneworld models can exhibit good agreement with large-scale structure observations [76, 108]. However, it has been noted in ref. [109] that the ISW and galaxy cross-correlation can become negative in the phantom braneworld scenario in presence of a brane tension, which can be used as a key signature of the braneworld scenario. In this context, we note that our typical best-fit values of $\Omega_{0\ell} \simeq 0.013$ lie within the constraint $\Omega_{0\ell} \lesssim 0.02$ derived in ref. [109] using the parametrized post-Friedmann framework. Nonetheless, a rigorous and updated treatment that incorporates the most recent observational datasets — including those from DESI DR2, Type Ia supernovae, and CMB — would require a separate study which we intend to undertake in a future work. In the meantime, the next DESI (DR3) data release is anticipated to deliver even tighter constraints on the evolution of dark energy.

JCAP11(2025)018

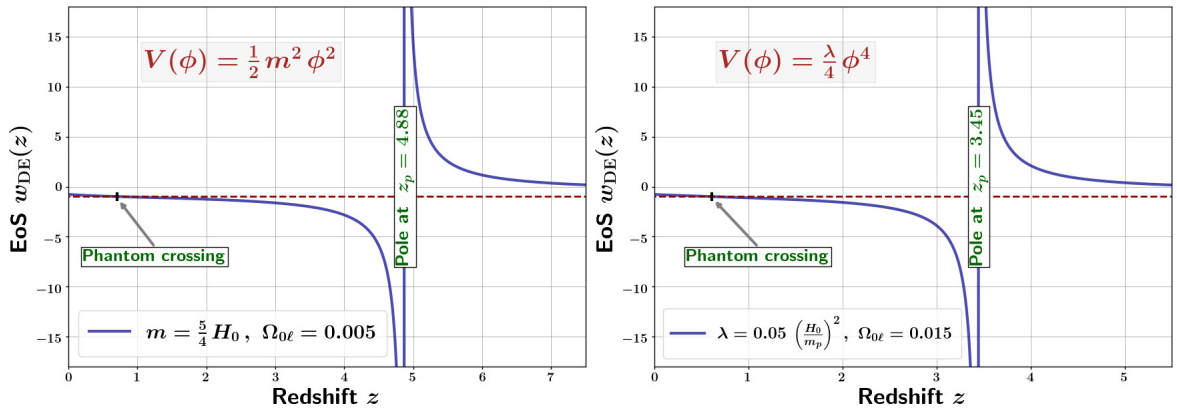

Figure 19. Figure displays the redshift location of the pole in the effective EoS of DE on the phantom brane at a relatively higher redshift, for the quadratic potential (3.1) in the *left panel* and for the quartic potential (3.2) in the *right panel*.

Acknowledgments

We thank Edmund Copeland for useful comments on the manuscript. SSM thanks Antonio Padilla for helpful discussions on the axion potential, and for comments on the braneworld model. We thank Rikpratik Sengupta for discussions during the early stages of this project. SSM is supported by a STFC Consolidated Grant [No. ST/T000732/1] as a Research Fellow at the University of Nottingham, U.K.. VS thanks Anusandhan National Research Foundation (ANRF), India, for the National Science Chair Professorship which provided partial funding for this work. YS is supported by the National Academy of Sciences of Ukraine under project 0121U109612 and by a grant from Simons Foundation International SFI-PD-Ukraine-00014573, PI LB. SSM thanks IUCAA for the hospitality during the conception phase of the project.

A Analytical estimate of the pole location

It is well-known that the effective EoS of DE on the phantom brane exhibits a pole [45] at a redshift where $\Omega_m(z) = 1$, as can be inferred from eq. (2.11). Location of the pole depends on $\Omega_{0\ell}$, and for relatively small values of $\Omega_{0\ell}$, the pole is usually located at a higher redshift. For the choice of parameters appearing in the figures of section 3, the corresponding pole is located at $z_p > 3$, which is outside the observational range of the DESI mission. figure 19 highlights the location of the pole for the quadratic (left panel) and quartic (right panel) potentials. In this appendix, we derive an analytical expression for determining the (approximate) location of the pole.

We can determine the redshift location of the pole as follows. Eq. (2.2) can be written as

$$1 + \sqrt{\Omega_\ell} = \sqrt{\Omega_m + \Omega_\phi + \Omega_\ell}\,, \tag{A.1}$$

where

$$\Omega_m = \frac{\Omega_{0m}}{h^2}\,, \qquad \Omega_\phi = \frac{\rho_\phi}{3m_p^2 H_0^2}\,\frac{1}{h^2}\,, \qquad \Omega_\ell = \frac{\Omega_{0\ell}}{h^2}\,. \tag{A.2}$$

Upon squaring both sides of eq. (A.1), we obtain

$$1 = \Omega_m + \Omega_\phi - 2\sqrt{\Omega_\ell}\,. \tag{A.3}$$

JCAP11(2025)018

Interpreting the above equation in the framework of GR as a Friedmann equation of the form

$$1 = \Omega_m + \Omega_{\rm DE}\,, \tag{A.4}$$

yields

$$\Omega_{\rm DE} = \Omega_\phi - 2\,\sqrt{\Omega_\ell}\,. \tag{A.5}$$

The location z_p of the pole in the effective EoS of DE can be inferred from eq. (2.11), by considering

$$\Omega_m = 1 \;\Rightarrow\; \Omega_{\rm DE} = 0\,,$$

which, using eq. (A.5), leads to

$$\Omega_\phi = 2\,\sqrt{\Omega_\ell}\,, \tag{A.6}$$

or, equivalently,

$$h = \frac{1}{2}\left(\frac{\rho_\phi}{3m_p^2H_0^2}\right)\frac{1}{\sqrt{\Omega_{0\ell}}}\,.$$

Since, at the location of the pole, $\Omega_{\rm DE} = 0$, and $\Omega_m = 1$, we have $h^2 = \Omega_{0m}\,(1+z_p)^3$, which results in

$$(1+z_p)^{3/2} = \frac{1}{2}\left(\frac{\rho_\phi}{3m_p^2H_0^2}\right)\left(\frac{1}{\sqrt{\Omega_{0\ell}\,\Omega_{0m}}}\right)\,, \tag{A.7}$$

leading to the final expression for the redshift location of the pole:

$$z_p = \left[\frac{1}{4}\left(\frac{\rho_\phi}{3m_p^2H_0^2}\right)^2\frac{1}{\Omega_{0\ell}\,\Omega_{0m}}\right]^{1/3} - 1\,. \tag{A.8}$$

If we constrain ourselves to the specific range of parameter space of the scalar field potential for which ϕ is still frozen at the epoch when the pole appears, i.e. $\phi(z_p) \simeq \phi_i$, then we can approximate ρ_ϕ as $\rho_\phi(z_p) = \rho_{\phi,i}$. In this case, the redshift location of the pole can be approximated as

$$z_p \simeq \left[\frac{1}{4}\,\frac{\Omega_{\phi,i}^2}{\Omega_{0\ell}\,\Omega_{0m}}\right]^{1/3} - 1\,. \tag{A.9}$$

Moreover, since ρ_ϕ will eventually start decreasing with time, we can write $\rho_{0\phi} = \xi\,\rho_{\phi,i}$ where $\xi \leq 1$ is a fraction. In terms of ξ, eq. (A.9) becomes

$$z_p \simeq \left[\frac{1}{4\,\xi^2}\,\frac{\Omega_{0\phi}^2}{\Omega_{0\ell}\,\Omega_{0m}}\right]^{1/3} - 1\,, \tag{A.10}$$

which demonstrates that, for higher values of $\Omega_{0\ell}$ (with all other parameters being the same), the pole appears at lower redshifts. The pole disappears in the GR limit $\Omega_{0l} \to 0$. For the choice of parameters appearing in the figures of section 3, the above formula is a good

JCAP11(2025)018

approximation, and yields a pole at $z_p > 3$, which is outside the observational range of the DESI mission. Note also, that for $\xi = 1$, the above eq. (A.10) agrees with eq. (15) of ref. [47].

However, for the choice of parameters where the scalar field has already started rolling down its potential by the redshift $z = z_p$ (or equivalently, when $\Omega_m = 1$), the approximation eq. (A.10) becomes inaccurate, and one needs to determine $\rho_\phi(z)$ numerically in order to obtain the value of z_p more accurately, using eq. (A.8). Nevertheless, eq. (A.8) demonstrates that if ρ_ϕ is smaller than $\rho_{\phi,i}$, then the pole appears at a lower redshift than what one would infer from eq. (A.10).

Before concluding this section, it is worth mentioning that, depending upon the functional form of the potential, a second pole in the EoS of DE might appear in the future, if $\Omega_{\rm DE}(z_p) = 0$ at some $z_p < 0$. Or equivalently, from eq. (2.7), if $\rho_\phi(z_p) = 3m_p^2 H_0^2 \sqrt{\Omega_{0\ell}}\, h(z_p)$ at some $z_p < 0$. Incidentally, this occurs for all the thawing potentials studied in this work. As mentioned before, two poles in the effective EoS of DE also appear in the coupled matter-quintessence model in GR studied in ref. [59]. However, since the second pole is located in the future in our scenario, it does not carry much significance from the observational perspective, and hence we do not discuss it further in this work.

B Evolution of other physical quantities in our models

In section 3, we displayed plots for the Hubble parameter and the effective EoS of DE for various models considered in this work. In this appendix, we include plots for the evolution of the DE fraction (2.10), deceleration parameter (2.9) and Om diagnostic (1.2) corresponding to each potential.

JCAP11(2025)018

B.1 Quadratic potential

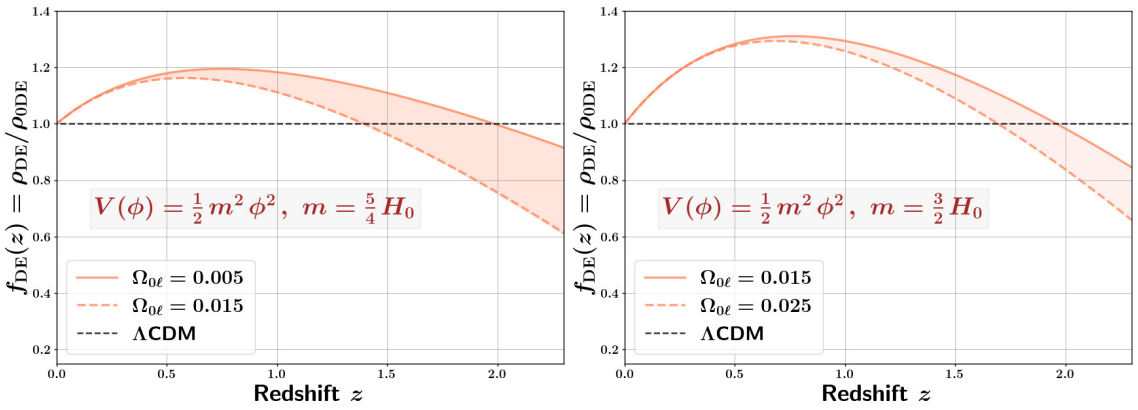

Figure 20. The DE density relative to its present-epoch value corresponding to the quadratic potential (3.1) is shown for $m = \frac{5}{4}H_0$ (*left panel*), and for $m = \frac{3}{2}H_0$ (*right panel*).

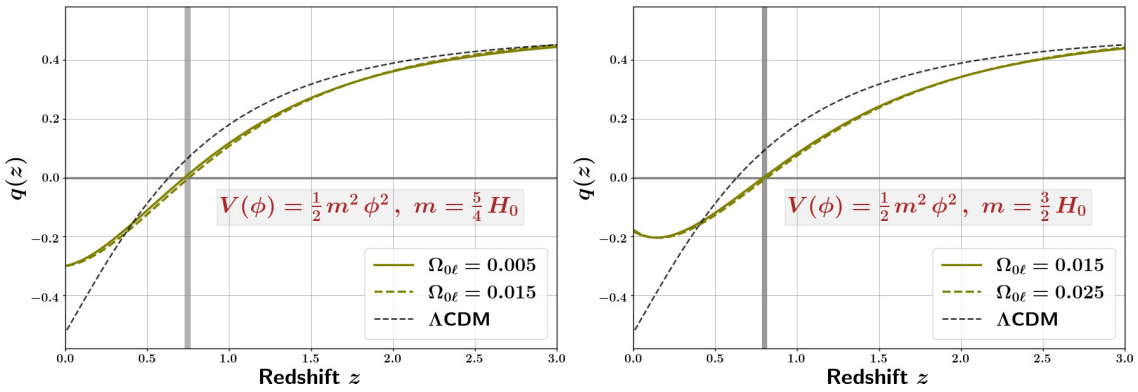

Figure 21. The deceleration parameter corresponding to the quadratic potential (3.1) is shown for $m = \frac{5}{4}H_0$ (*left panel*), and for $m = \frac{3}{2}H_0$ (*right panel*).

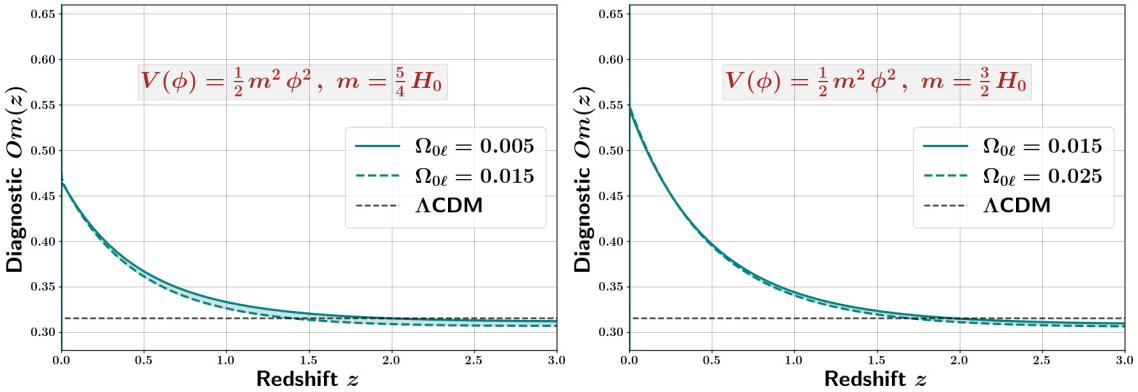

Figure 22. The Om diagnostic parameter corresponding to the quadratic potential (3.1) is shown for $m = \frac{5}{4}H_0$ (*left panel*), and for $m = \frac{3}{2}H_0$ (*right panel*).

JCAP11(2025)018

B.2 Quartic potential

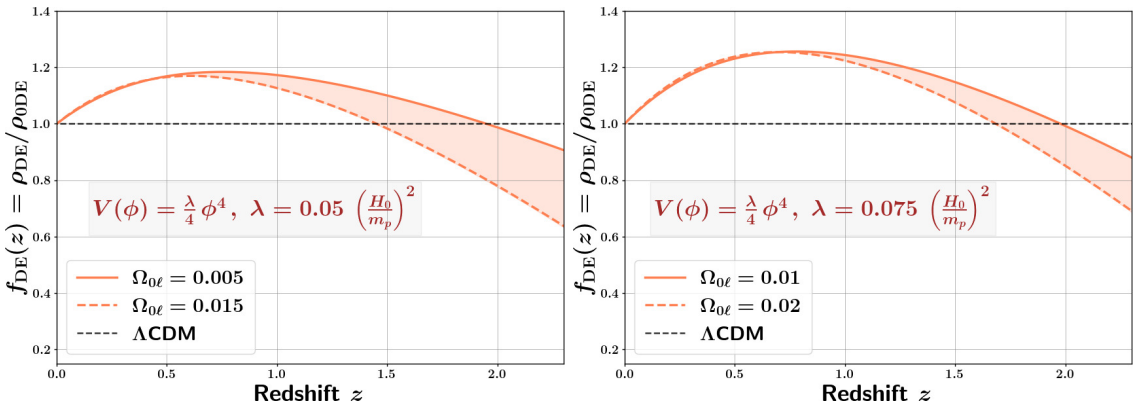

Figure 23. The DE density relative to its present-epoch value for the quartic potential (3.2) are shown for $\lambda = 0.05\,(H_0/m_p)^2$ (*left panel*), and for $\lambda = 0.075\,(H_0/m_p)^2$ (*right panel*).

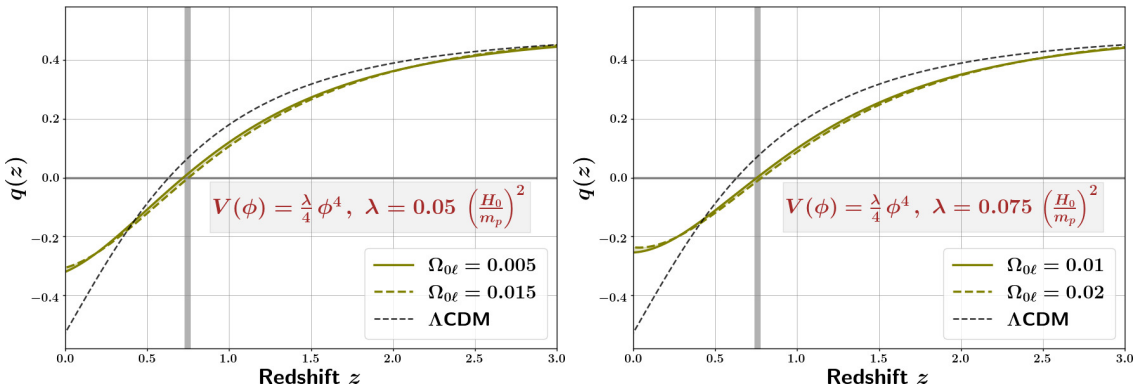

Figure 24. The deceleration parameter corresponding to the quartic potential (3.2) is shown for $\lambda = 0.05\,(H_0/m_p)^2$ (*left panel*), and for $\lambda = 0.075\,(H_0/m_p)^2$ (*right panel*).

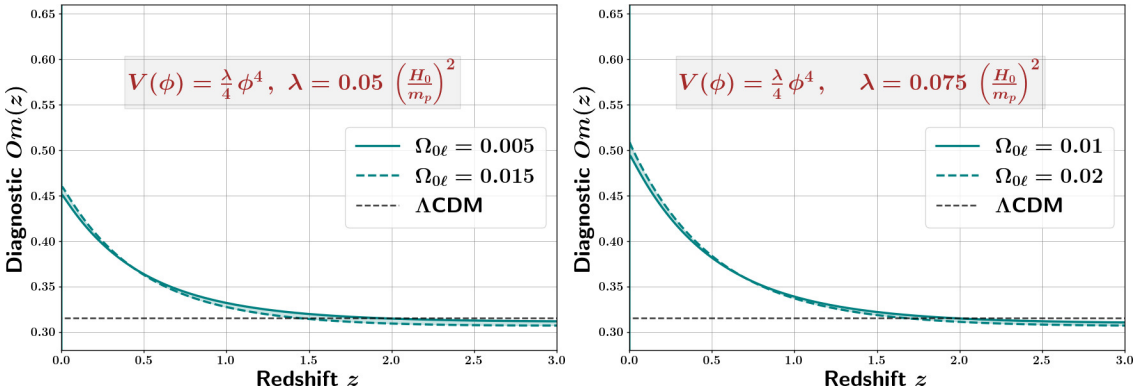

Figure 25. The Om diagnostic parameter corresponding to the quartic potential (3.2) is shown for $\lambda = 0.05\,(H_0/m_p)^2$ (*left panel*), and for $\lambda = 0.075\,(H_0/m_p)^2$ (*right panel*).

JCAP11(2025)018

B.3 Symmetry-breaking potential: steep wing

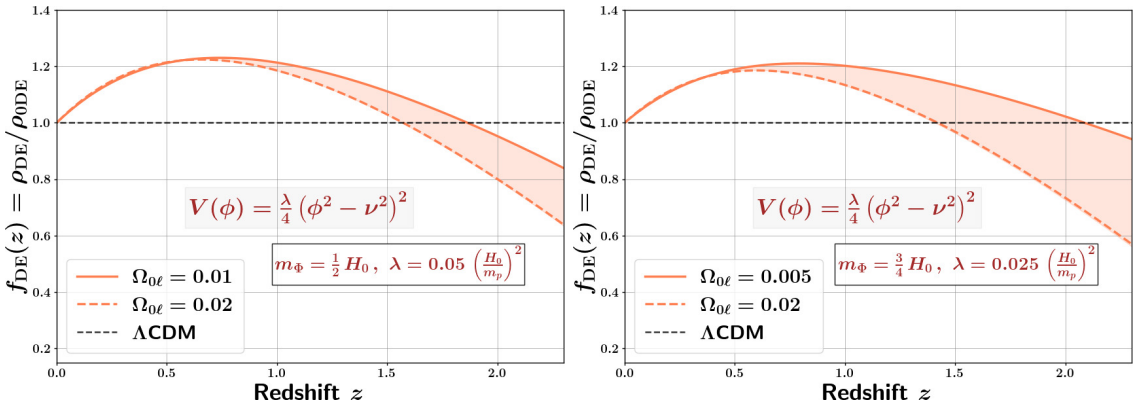

Figure 26. The DE density relative to its present-epoch value corresponding to the steep right wing of the symmetry-breaking potential (3.3) are shown for $m_\Phi = \frac{1}{2}H_0\,,\ \lambda = 0.05\,(H_0/m_p)^2$ (*left panel*), and for $m_\Phi = \frac{3}{4}H_0\,,\ \lambda = 0.025\,(H_0/m_p)^2$ (*right panel*).

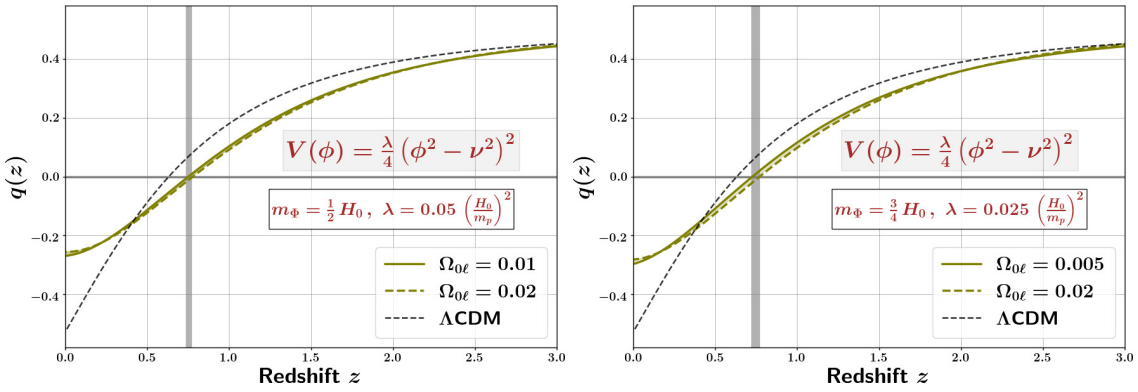

Figure 27. The deceleration parameter corresponding to the steep right wing of the symmetry-breaking potential (3.3) is shown for $m_\Phi = \frac{1}{2}H_0\,,\ \lambda = 0.05\,(H_0/m_p)^2$ (*left panel*), and for $m_\Phi = \frac{3}{4}H_0\,,\ \lambda = 0.025\,(H_0/m_p)^2$ (*right panel*).

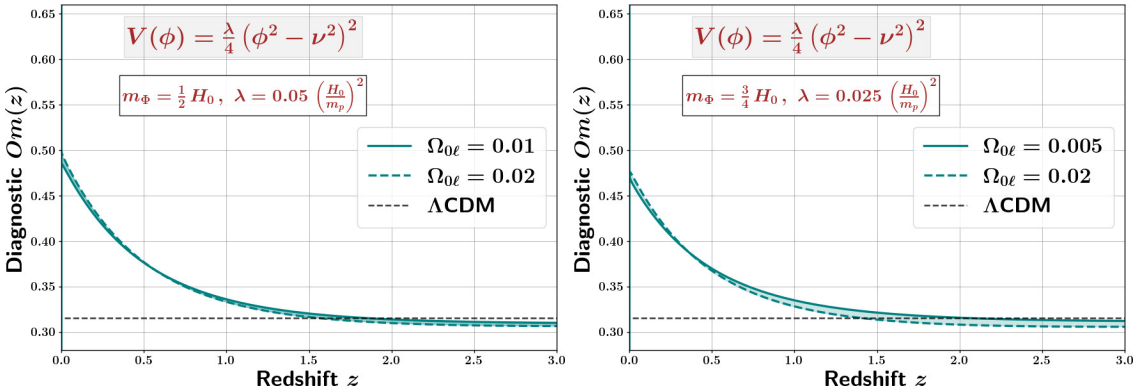

Figure 28. The Om diagnostic parameter corresponding to the steep right wing of the symmetry-breaking potential (3.3) is shown for $m_\Phi = \frac{1}{2}H_0\,,\ \lambda = 0.05\,(H_0/m_p)^2$ (*left panel*), and for $m_\Phi = \frac{3}{4}H_0\,,\ \lambda = 0.025\,(H_0/m_p)^2$ (*right panel*).

JCAP11(2025)018

B.4 Symmetry-breaking potential: flat wing

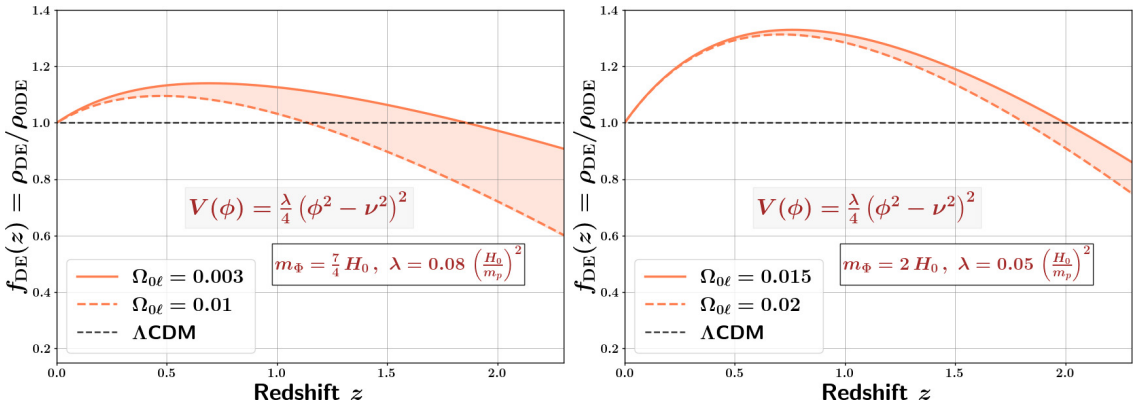

Figure 29. The DE density relative to its present-epoch value corresponding to the flat left wing of the symmetry-breaking potential (3.3) is shown for $m_\Phi = \frac{7}{4}\,H_0\,,\ \lambda = 0.08\,(H_0/m_p)^2$ (*left panel*), and for $m_\Phi = 2\,H_0\,,\ \lambda = 0.05\,(H_0/m_p)^2$ (*right panel*).

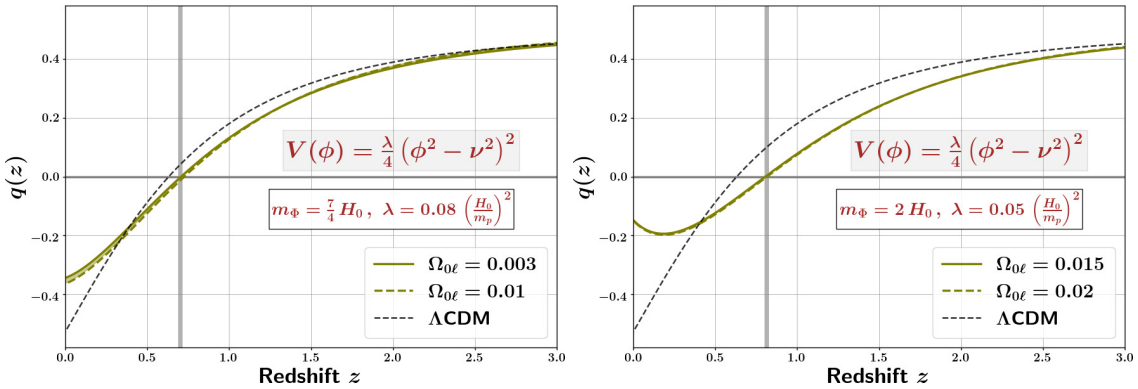

Figure 30. The deceleration parameter corresponding to the flat left wing of the symmetry-breaking potential (3.3) is shown for $m_\Phi = \frac{7}{4}\,H_0\,,\ \lambda = 0.08\,(H_0/m_p)^2$ (*left panel*), and for $m_\Phi = 2\,H_0\,,\ \lambda = 0.05\,(H_0/m_p)^2$ (*right panel*).

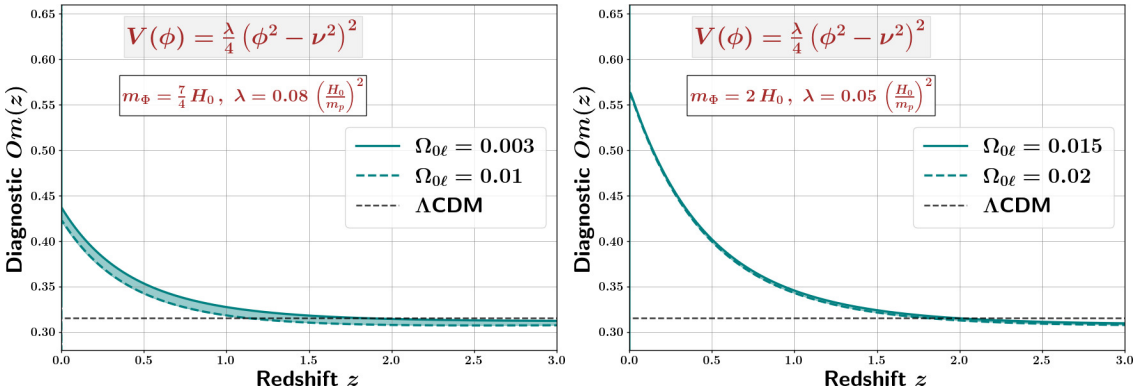

Figure 31. The Om diagnostic parameter corresponding to the flat left wing of the symmetry-breaking potential (3.3) is shown for $m_\Phi = \frac{7}{4}\,H_0\,,\ \lambda = 0.08\,(H_0/m_p)^2$ (*left panel*), and for $m_\Phi = 2\,H_0\,,\ \lambda = 0.05\,(H_0/m_p)^2$ (*right panel*).

JCAP11(2025)018

B.5 Exponential potential

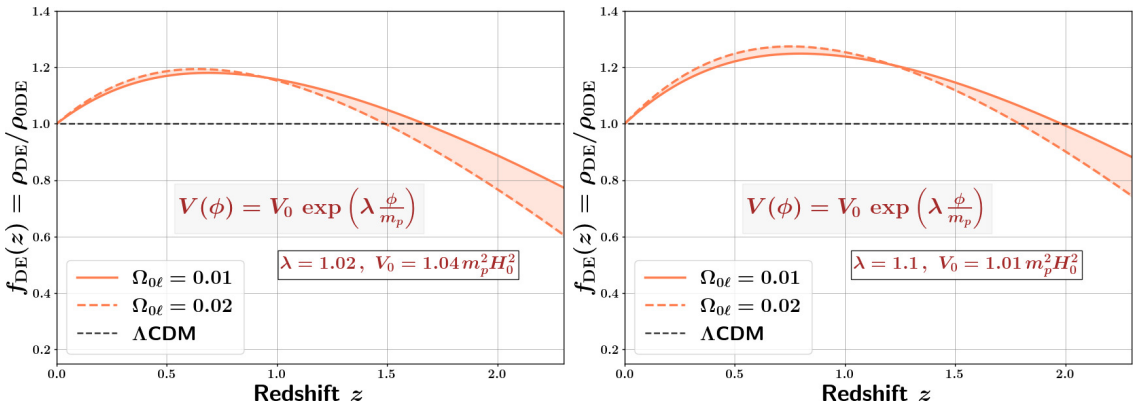

Figure 32. The DE density relative to its present-epoch value for the exponential potential (3.7) is shown for $\lambda = 1.02$, $V_0 = 1.04\, m_p^2 H_0^2$ (*left panel*), and for $\lambda = 1.1$, $V_0 = 1.01\, m_p^2 H_0^2$ (*right panel*).

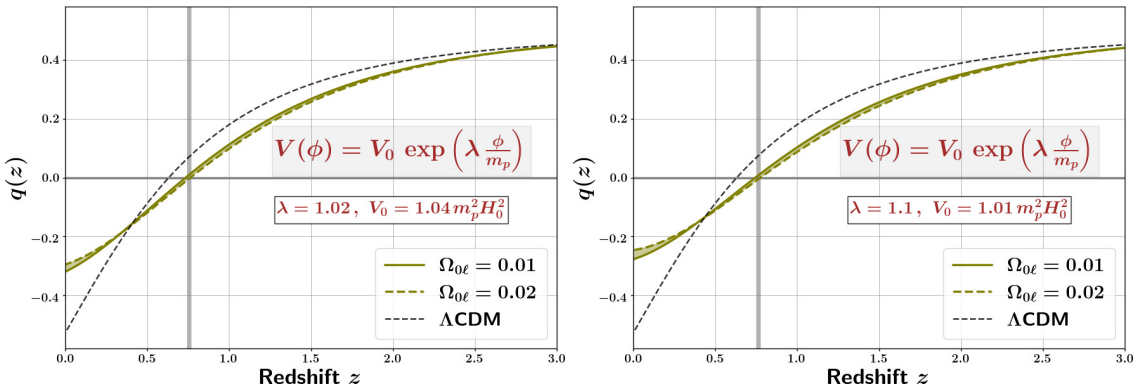

Figure 33. The deceleration parameter for the exponential potential (3.7) is shown for $\lambda = 1.02$, $V_0 = 1.04\, m_p^2 H_0^2$ (*left panel*), and for $\lambda = 1.1$, $V_0 = 1.01\, m_p^2 H_0^2$ (*right panel*).

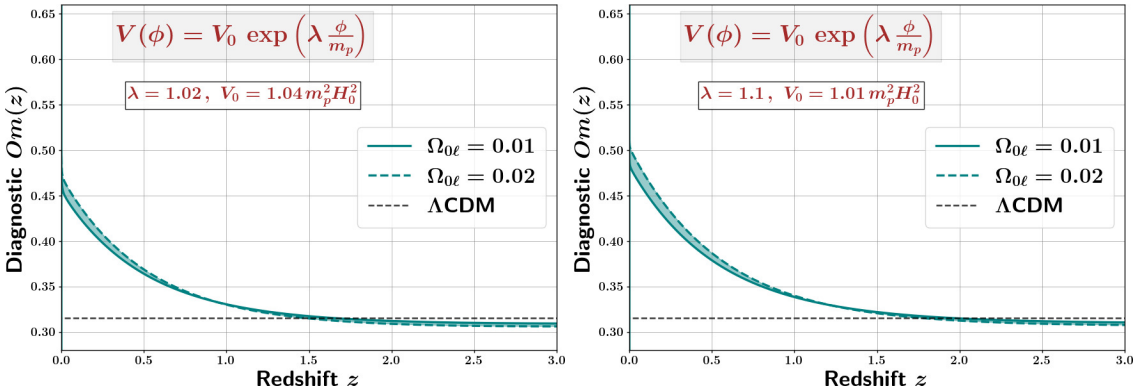

Figure 34. The Om diagnostic parameter for the exponential potential (3.7) is shown for $\lambda = 1.02$, $V_0 = 1.04\, m_p^2 H_0^2$ (*left panel*), and for $\lambda = 1.1$, $V_0 = 1.01\, m_p^2 H_0^2$ (*right panel*).

JCAP11(2025)018

B.6 Axion potential

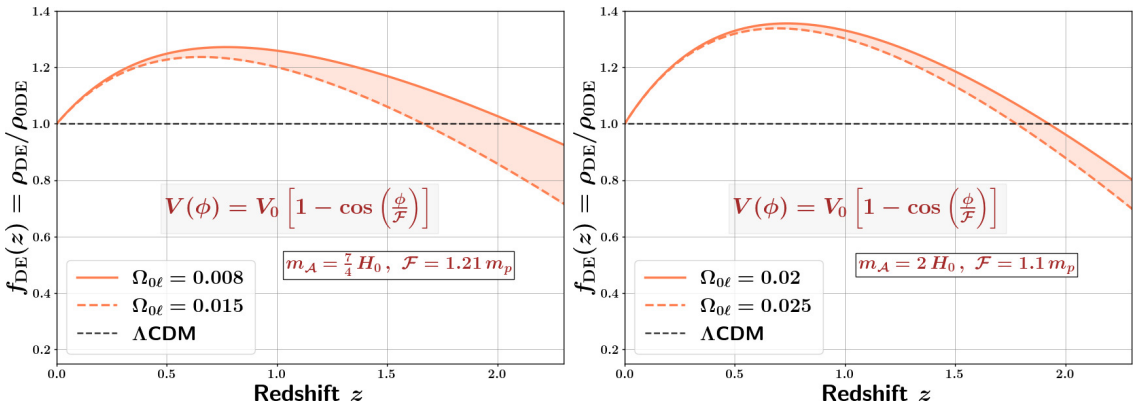

Figure 35. The DE density relative to its present-epoch value for the Axion potential (3.8) is shown for $m_{\mathcal{A}} = \frac{7}{4}\, H_0\,,\ \mathcal{F} = 1.21\, m_p$ (*left panel*), and for $m_{\mathcal{A}} = 2\, H_0\,,\ \mathcal{F} = 1.1\, m_p$ (*right panel*).

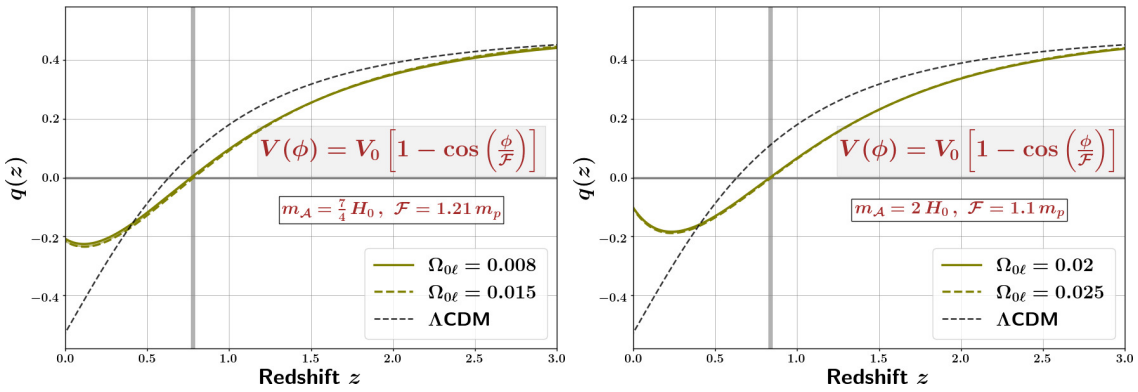

Figure 36. The deceleration parameter corresponding to the Axion potential (3.8) is shown for $m_{\mathcal{A}} = \frac{7}{4}\, H_0\,,\ \mathcal{F} = 1.21\, m_p$ (*left panel*), and for $m_{\mathcal{A}} = 2\, H_0\,,\ \mathcal{F} = 1.1\, m_p$ (*right panel*).

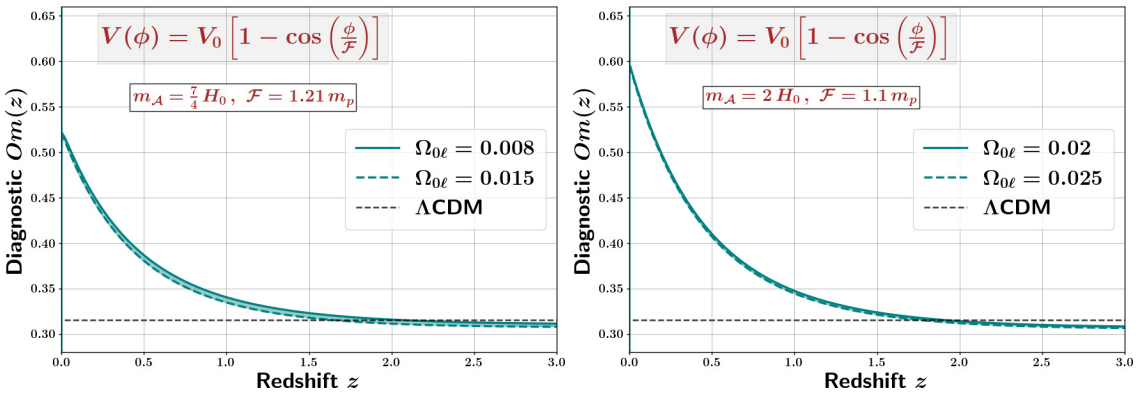

Figure 37. The Om diagnostic parameter for the Axion potential (3.8) is shown for $m_{\mathcal{A}} = \frac{7}{4}\, H_0\,,\ \mathcal{F} = 1.21\, m_p$ (*left panel*), and for $m_{\mathcal{A}} = 2\, H_0\,,\ \mathcal{F} = 1.1\, m_p$ (*right panel*).

JCAP11(2025)018

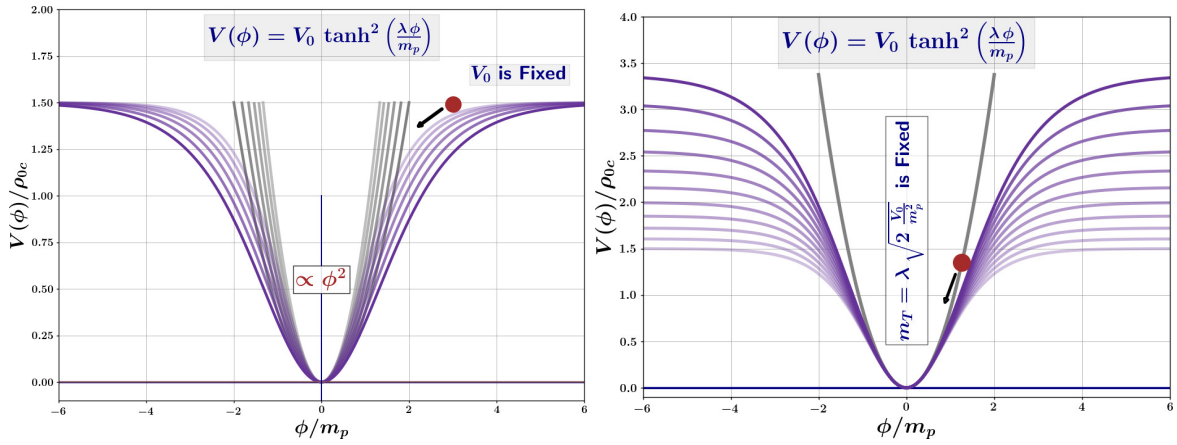

Figure 38. A schematic plot of the plateau potential, given in eq. (C.1), is shown by the purple curves: the *left panel* illustrates the potential for a fixed value of V_0 and varying λ, while the *right panel* shows it for a fixed m_T and varying V_0. The quadratic approximation [eq. (C.2)] is indicated by the light-gray curves.

C Plateau potential

Consider the plateau potential[14] given by

$$V(\phi) = V_0 \tanh^2\left(\lambda\,\frac{\phi}{m_p}\right), \tag{C.1}$$

which is naturally stabilised at the minimum, and exhibits asymptotically flat behaviour for $\phi \gg \lambda/m_p$, see figure 38.

Note that, for $\phi \ll m_p/\lambda$, the potential can be approximated as a quadratic potential up to leading order in $\lambda\,\phi/m_p$, that is,

$$V(\phi)\big|_{\phi \ll m_p/\lambda} \simeq \frac{1}{2}\,m_T^2\,\phi^2 - \mathcal{O}\left(\frac{\lambda\,\phi}{m_p}\right)^4, \tag{C.2}$$

with

$$m_T = \lambda\sqrt{\frac{2\,V_0}{m_p^2}} \quad \Rightarrow \quad \frac{m_T}{H_0} = \lambda\sqrt{\frac{6\,V_0}{3\,m_p^2\,H_0^2}}\,. \tag{C.3}$$

We perform numerical simulations for a range of (fixed) values of m_T. Our results are illustrated in figure 39–43. The plots are generated for two distinct values of the scalar field mass, namely $m_T = 2H_0$, and $\frac{9}{4}H_0$, while keeping the value of V_0 fixed.

Note that the value of m_T is a function of V_0 and λ, as given by eq. (C.3). To ensure a minimum required amount of dark energy at present, V_0 must exceed a certain critical value. For a fixed mass, choosing a very large V_0 necessitates a correspondingly small λ. In this limit, the dark energy dynamics of the plateau potential closely resembles that of a purely quadratic potential; see the right panel of figure 38.

[14]The *plateau* potential is popularly known as the T-Model α-attractor potential [110] in the context of inflation.

JCAP11(2025)018

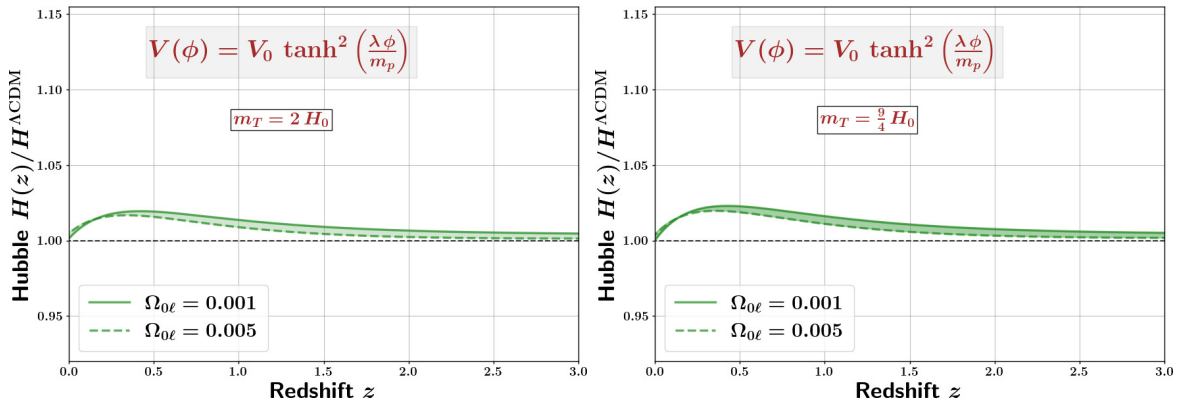

Figure 39. The Hubble parameter corresponding to the plateau potential (C.1) is shown for $m_T = 2\,H_0$ (*left panel*), and $m_T = \frac{9}{4}\,H_0$ (*right panel*).

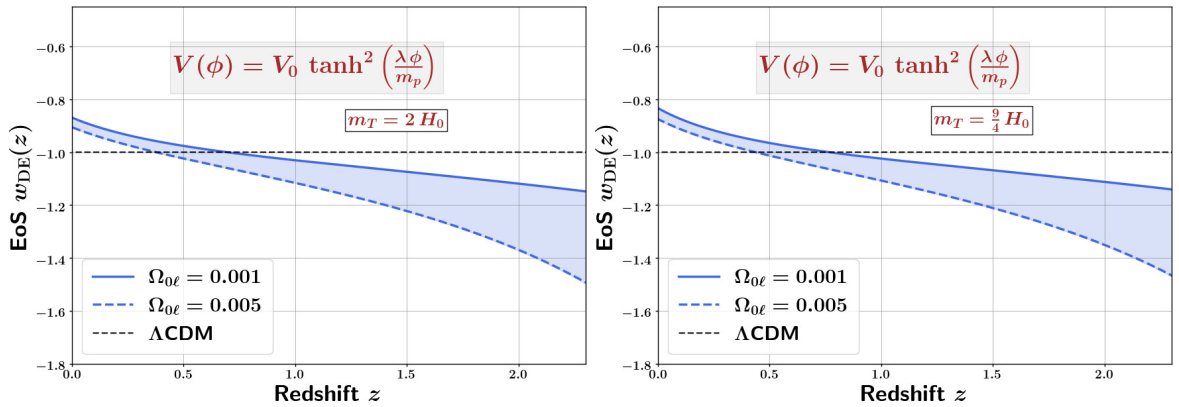

Figure 40. The DE equation-of-state parameter corresponding to the plateau potential (C.1) is shown for $m_T = 2\,H_0$ (*left panel*), and for $m_T = \frac{9}{4}\,H_0$ (*right panel*).

Therefore, we consider the opposite limit by setting $V_0 = \frac{9}{2}m_p^2H_0^2$, which is sufficiently small to allow a given scalar field mass to be achieved with a correspondingly large value of λ. In this regime, the dynamics is expected to exhibit a significant deviation from the purely quadratic case — which is precisely what we observe.

A visual comparison of our plots with those of ref. [33] indicate that the DESI DR2 constraints appear to be somewhat consistent with a plateau potential on the phantom brane for the parameters chosen in figure 39–43.

This potential appears to perform less effectively than the ones discussed in section 3 because the results are displayed for $V_0 = \frac{9}{2}m_p^2H_0^2$, as highlighted in the previous paragraph. If we had chosen higher values of V_0, then our results would have resembled those of the quadratic potential, which more consistent with the DESI DR2 data.

JCAP11(2025)018

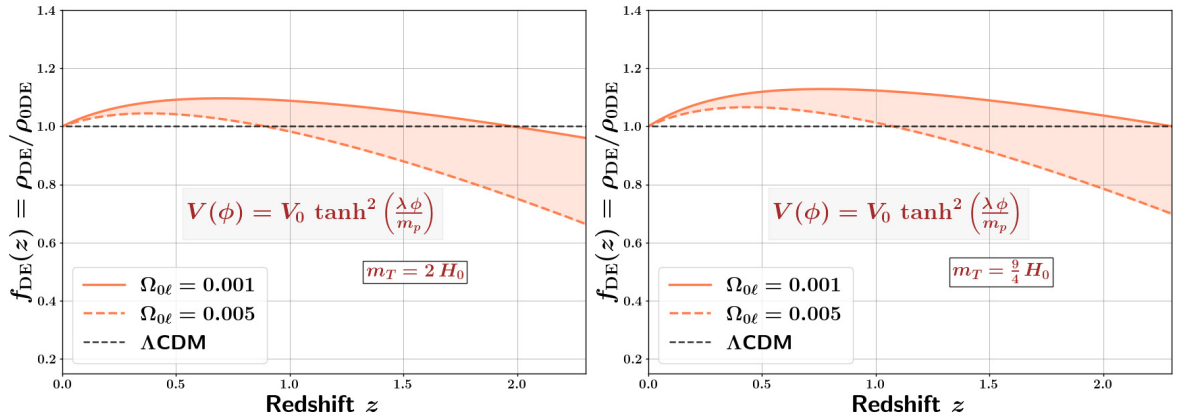

Figure 41. The DE density relative to its present-epoch value corresponding to the plateau potential (C.1) is shown for $m_T = 2\,H_0$ (*left panel*), and for $m_T = \frac{9}{4}\,H_0$ (*right panel*).

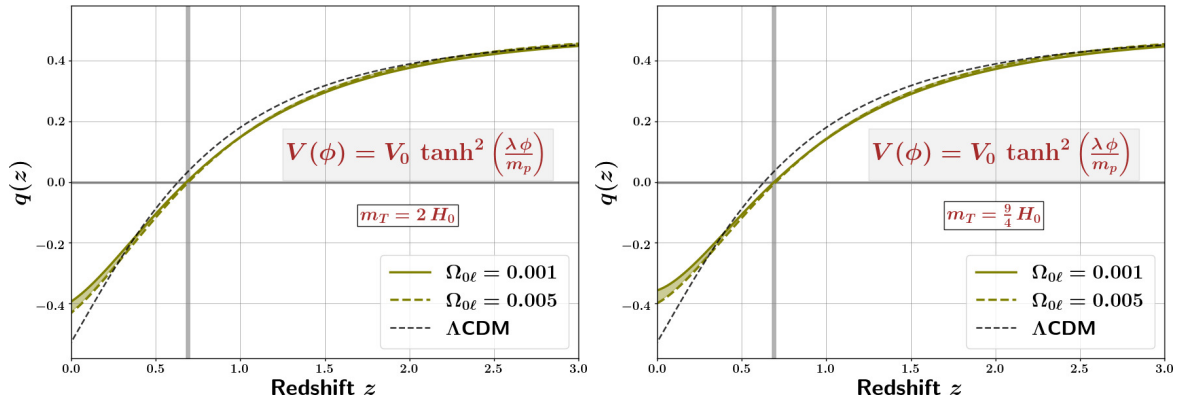

Figure 42. The deceleration parameter corresponding to the plateau potential (C.1) is shown for $m_T = 2\,H_0$ (*left panel*), and for $m_T = \frac{9}{4}\,H_0$ (*right panel*).

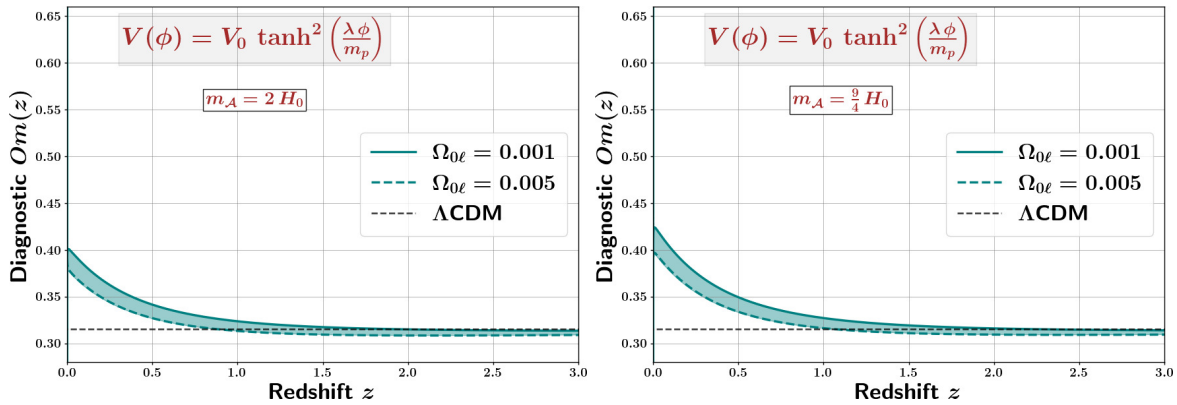

Figure 43. The Om diagnostic parameter corresponding to the plateau potential (C.1) is shown for $m_T = 2\,H_0$ (*left panel*), and for $m_T = \frac{9}{4}\,H_0$ (*right panel*).

JCAP11(2025)018

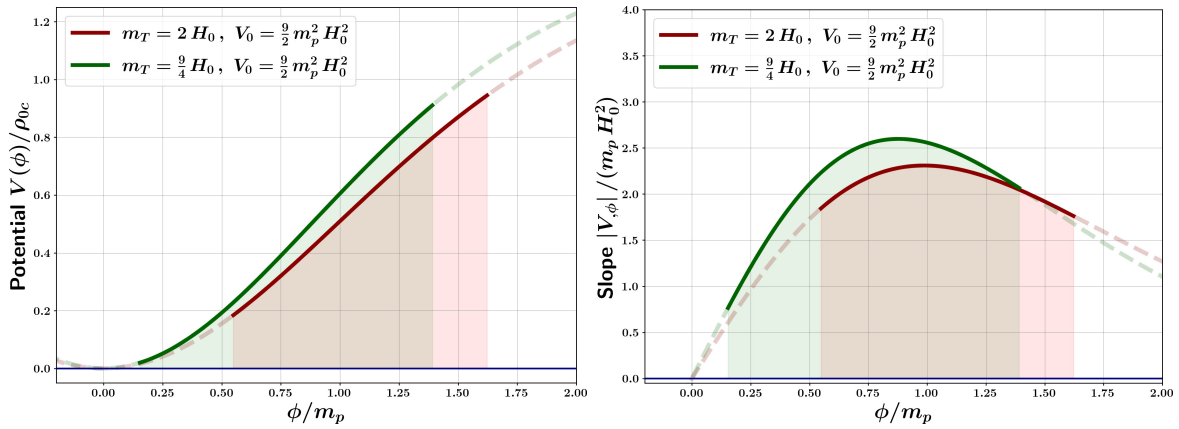

Figure 44. *Left panel* shows the plateau potential (C.1) with $V_0 = \frac{9}{2}\,m_p^2\,H_0^2$, along with $m_T = 2\,H_0$ (red) and $m_T = \frac{9}{4}\,H_0$ (green). The *right panel* shows the corresponding slopes. The *darker (solid) curves* with vertical shades correspond to the field (ϕ) range explored during the full simulation time, i.e. from $z = 99$ to $z \lesssim -1$. The *fainter (dashed) curves* correspond to a much wider range of values of ϕ.

References

[1] Supernova Search Team collaboration, *Observational evidence from supernovae for an accelerating universe and a cosmological constant*, *Astron. J.* **116** (1998) 1009 [astro-ph/9805201] [INSPIRE].

[2] Supernova Cosmology Project collaboration, *Measurements of Ω and Λ from 42 high redshift supernovae*, *Astrophys. J.* **517** (1999) 565 [astro-ph/9812133] [INSPIRE].

[3] Y.B. Zel'dovich, A. Krasinski and Y.B. Zeldovich, *The cosmological constant and the theory of elementary particles*, *Sov. Phys. Usp.* **11** (1968) 381 [INSPIRE].

[4] S. Weinberg, *The cosmological constant problem*, *Rev. Mod. Phys.* **61** (1989) 1 [INSPIRE].

[5] B. Ratra and P.J.E. Peebles, *Cosmological consequences of a rolling homogeneous scalar field*, *Phys. Rev. D* **37** (1988) 3406 [INSPIRE].

[6] P.J.E. Peebles and B. Ratra, *Cosmology with a time variable cosmological constant*, *Astrophys. J. Lett.* **325** (1988) L17 [INSPIRE].

[7] V. Sahni and A.A. Starobinsky, *The case for a positive cosmological Lambda term*, *Int. J. Mod. Phys. D* **9** (2000) 373 [astro-ph/9904398] [INSPIRE].

[8] P.J.E. Peebles and B. Ratra, *The cosmological constant and dark energy*, *Rev. Mod. Phys.* **75** (2003) 559 [astro-ph/0207347] [INSPIRE].

[9] T. Padmanabhan, *Cosmological constant: the weight of the vacuum*, *Phys. Rept.* **380** (2003) 235 [hep-th/0212290] [INSPIRE].

[10] V. Sahni, *Dark matter and dark energy*, in *The physics of the early universe*, Springer, Berlin, Heidelberg, Germany (2004), p. 141–179 [DOI:10.1007/978-3-540-31535-3_5].

[11] E.J. Copeland, M. Sami and S. Tsujikawa, *Dynamics of dark energy*, *Int. J. Mod. Phys. D* **15** (2006) 1753 [hep-th/0603057] [INSPIRE].

[12] R. Bousso, *TASI lectures on the cosmological constant*, *Gen. Rel. Grav.* **40** (2008) 607 [arXiv:0708.4231] [INSPIRE].

JCAP11(2025)018

[13] J. Frieman, M. Turner and D. Huterer, *Dark energy and the accelerating universe*, *Ann. Rev. Astron. Astrophys.* **46** (2008) 385 [arXiv:0803.0982] [INSPIRE].

[14] R. Durrer and R. Maartens, *Dark energy and modified gravity*, arXiv:0811.4132 [INSPIRE].

[15] M. Li, X.-D. Li, S. Wang and Y. Wang, *Dark energy*, *Commun. Theor. Phys.* **56** (2011) 525 [arXiv:1103.5870] [INSPIRE].

[16] S. Nojiri and S.D. Odintsov, *Unified cosmic history in modified gravity: from F(R) theory to Lorentz non-invariant models*, *Phys. Rept.* **505** (2011) 59 [arXiv:1011.0544] [INSPIRE].

[17] T. Clifton, P.G. Ferreira, A. Padilla and C. Skordis, *Modified gravity and cosmology*, *Phys. Rept.* **513** (2012) 1 [arXiv:1106.2476] [INSPIRE].

[18] L. Amendola and S. Tsujikawa, *Dark energy: theory and observations*, Cambridge University Press, Cambridge, U.K. (2015).

[19] A. Padilla, *Lectures on the cosmological constant problem*, arXiv:1502.05296 [INSPIRE].

[20] V. Sahni and A. Starobinsky, *Reconstructing dark energy*, *Int. J. Mod. Phys. D* **15** (2006) 2105 [astro-ph/0610026] [INSPIRE].

[21] M. Chevallier and D. Polarski, *Accelerating universes with scaling dark matter*, *Int. J. Mod. Phys. D* **10** (2001) 213 [gr-qc/0009008] [INSPIRE].

[22] E.V. Linder, *Exploring the expansion history of the universe*, *Phys. Rev. Lett.* **90** (2003) 091301 [astro-ph/0208512] [INSPIRE].

[23] V. Sahni, A. Shafieloo and A.A. Starobinsky, *Two new diagnostics of dark energy*, *Phys. Rev. D* **78** (2008) 103502 [arXiv:0807.3548] [INSPIRE].

[24] C. Zunckel and C. Clarkson, *Consistency tests for the cosmological constant*, *Phys. Rev. Lett.* **101** (2008) 181301 [arXiv:0807.4304] [INSPIRE].

[25] V. Sahni, A. Shafieloo and A.A. Starobinsky, *Model independent evidence for dark energy evolution from Baryon Acoustic Oscillations*, *Astrophys. J. Lett.* **793** (2014) L40 [arXiv:1406.2209] [INSPIRE].

[26] DESI collaboration, *DESI 2024 III: baryon acoustic oscillations from galaxies and quasars*, *JCAP* **04** (2025) 012 [arXiv:2404.03000] [INSPIRE].

[27] DESI collaboration, *DESI 2024 IV: baryon acoustic oscillations from the Lyman α forest*, *JCAP* **01** (2025) 124 [arXiv:2404.03001] [INSPIRE].

[28] DESI collaboration, *Data release 1 of the Dark Energy Spectroscopic Instrument*, arXiv:2503.14745 [INSPIRE].

[29] DESI collaboration, *DESI 2024: constraints on physics-focused aspects of dark energy using DESI DR1 BAO data*, *Phys. Rev. D* **111** (2025) 023532 [arXiv:2405.13588] [INSPIRE].

[30] DESI collaboration, *DESI 2024 VI: cosmological constraints from the measurements of baryon acoustic oscillations*, *JCAP* **02** (2025) 021 [arXiv:2404.03002] [INSPIRE].

[31] DESI collaboration, *DESI 2024: reconstructing dark energy using crossing statistics with DESI DR1 BAO data*, *JCAP* **10** (2024) 048 [arXiv:2405.04216] [INSPIRE].

[32] DESI collaboration, *DESI 2024 VII: cosmological constraints from the full-shape modeling of clustering measurements*, *JCAP* **07** (2025) 028 [arXiv:2411.12022] [INSPIRE].

[33] DESI collaboration, *Extended dark energy analysis using DESI DR2 BAO measurements*, *Phys. Rev. D* **112** (2025) 083511 [arXiv:2503.14743] [INSPIRE].

JCAP11(2025)018

[34] M. Cortês and A.R. Liddle, *Interpreting DESI's evidence for evolving dark energy*, *JCAP* **12** (2024) 007 [arXiv:2404.08056] [INSPIRE].

[35] C.-G. Park, J. de Cruz Pérez and B. Ratra, *Is the w_0w_aCDM cosmological parameterization evidence for dark energy dynamics partially caused by the excess smoothing of Planck CMB anisotropy data?*, *Int. J. Mod. Phys. D* **34** (2025) 2550058 [arXiv:2410.13627] [INSPIRE].

[36] C.-G. Park and B. Ratra, *Is excess smoothing of Planck CMB anisotropy data partially responsible for evidence for dark energy dynamics in other $w(z)$CDM parametrizations?*, *Int. J. Mod. Phys. D* **34** (2025) 2550061 [arXiv:2501.03480] [INSPIRE].

[37] D. Wang and D. Mota, *Did DESI DR2 truly reveal dynamical dark energy?*, arXiv:2504.15222 [INSPIRE].

[38] A.N. Ormondroyd, W.J. Handley, M.P. Hobson and A.N. Lasenby, *Comparison of dynamical dark energy with ΛCDM in light of DESI DR2*, arXiv:2503.17342 [INSPIRE].

[39] M. Cortês and A.R. Liddle, *On DESI's DR2 exclusion of ΛCDM*, arXiv:2504.15336 [INSPIRE].

[40] S. Roy Choudhury and T. Okumura, *Updated cosmological constraints in extended parameter space with Planck PR4, DESI baryon acoustic oscillations, and supernovae: dynamical dark energy, neutrino masses, lensing anomaly, and the Hubble tension*, *Astrophys. J. Lett.* **976** (2024) L11 [arXiv:2409.13022] [INSPIRE].

[41] C.-G. Park, J. de Cruz Pérez and B. Ratra, *Using non-DESI data to confirm and strengthen the DESI 2024 spatially flat w0waCDM cosmological parametrization result*, *Phys. Rev. D* **110** (2024) 123533 [arXiv:2405.00502] [INSPIRE].

[42] S. Roy Choudhury, *Cosmology in extended parameter space with DESI data release 2 baryon acoustic oscillations: a $2\sigma+$ detection of nonzero neutrino masses with an update on dynamical dark energy and lensing anomaly*, *Astrophys. J. Lett.* **986** (2025) L31 [arXiv:2504.15340] [INSPIRE].

[43] M. Braglia, X. Chen and A. Loeb, *Exotic dark matter and the DESI anomaly*, arXiv:2507.13925 [INSPIRE].

[44] R.R. Caldwell and E.V. Linder, *The limits of quintessence*, *Phys. Rev. Lett.* **95** (2005) 141301 [astro-ph/0505494] [INSPIRE].

[45] V. Sahni and Y. Shtanov, *Brane world models of dark energy*, *JCAP* **11** (2003) 014 [astro-ph/0202346] [INSPIRE].

[46] A. Lue and G.D. Starkman, *How a brane cosmological constant can trick us into thinking that $W < -1$*, *Phys. Rev. D* **70** (2004) 101501 [astro-ph/0408246] [INSPIRE].

[47] U. Alam, S. Bag and V. Sahni, *Constraining the cosmology of the phantom brane using distance measures*, *Phys. Rev. D* **95** (2017) 023524 [arXiv:1605.04707] [INSPIRE].

[48] S. Bag, V. Sahni, A. Shafieloo and Y. Shtanov, *Phantom braneworld and the Hubble tension*, *Astrophys. J.* **923** (2021) 212 [arXiv:2107.03271] [INSPIRE].

[49] J.A. Frieman, C.T. Hill, A. Stebbins and I. Waga, *Cosmology with ultralight pseudo Nambu-Goldstone bosons*, *Phys. Rev. Lett.* **75** (1995) 2077 [astro-ph/9505060] [INSPIRE].

[50] W.J. Wolf, C. García-García, T. Anton and P.G. Ferreira, *Assessing cosmological evidence for nonminimal coupling*, *Phys. Rev. Lett.* **135** (2025) 081001 [arXiv:2504.07679] [INSPIRE].

[51] C. You, D. Wang and T. Yang, *Dynamical dark energy implies a coupled dark sector: insights from DESI DR2 via a data-driven approach*, *Phys. Rev. D* **112** (2025) 043503 [arXiv:2504.00985] [INSPIRE].

JCAP11(2025)018

[52] R. Shah, P. Mukherjee and S. Pal, *Interacting dark sectors in light of DESI DR2*, *Mon. Not. Roy. Astron. Soc.* **542** (2025) 2936 [arXiv:2503.21652] [INSPIRE].

[53] Y. Akrami, G. Alestas and S. Nesseris, *Has DESI detected exponential quintessence?*, arXiv:2504.04226 [INSPIRE].

[54] G. Ye and Y. Cai, *NEC violation and "beyond Horndeski" physics in light of DESI DR2*, arXiv:2503.22515 [INSPIRE].

[55] U.K. Tyagi, S. Haridasu and S. Basak, *Constraints on generalized gravity-thermodynamic cosmology from DESI DR2*, arXiv:2504.11308 [INSPIRE].

[56] U. Kumar, A. Ajith and A. Verma, *Evidence for non-cold dark matter from DESI DR2 measurements*, arXiv:2504.14419 [INSPIRE].

[57] DESI collaboration, *Positive neutrino masses with DESI DR2 via matter conversion to dark energy*, *Phys. Rev. Lett.* **135** (2025) 081003 [arXiv:2504.20338] [INSPIRE].

[58] I.D. Gialamas et al., *Quintessence and phantoms in light of DESI 2025*, *Phys. Rev. D* **112** (2025) 063551 [arXiv:2506.21542] [INSPIRE].

[59] D. Andriot, *Phantom matters*, *Phys. Dark Univ.* **49** (2025) 102000 [arXiv:2505.10410] [INSPIRE].

[60] M. Scherer, M.A. Sabogal, R.C. Nunes and A. De Felice, *Challenging the ΛCDM model: 5σ evidence for a dynamical dark energy late-time transition*, *Phys. Rev. D* **112** (2025) 043513 [arXiv:2504.20664] [INSPIRE].

[61] E. Silva et al., *New constraints on interacting dark energy from DESI DR2 BAO observations*, *Phys. Rev. D* **111** (2025) 123511 [arXiv:2503.23225] [INSPIRE].

[62] W.J. Wolf, P.G. Ferreira and C. García-García, *Matching current observational constraints with nonminimally coupled dark energy*, *Phys. Rev. D* **111** (2025) L041303 [arXiv:2409.17019] [INSPIRE].

[63] G. Ye, M. Martinelli, B. Hu and A. Silvestri, *Hints of nonminimally coupled gravity in DESI 2024 baryon acoustic oscillation measurements*, *Phys. Rev. Lett.* **134** (2025) 181002 [arXiv:2407.15832] [INSPIRE].

[64] W.J. Wolf, C. García-García and P.G. Ferreira, *Robustness of dark energy phenomenology across different parameterizations*, *JCAP* **05** (2025) 034 [arXiv:2502.04929] [INSPIRE].

[65] U. Alam, V. Sahni and A.A. Starobinsky, *Is dark energy decaying?*, *JCAP* **04** (2003) 002 [astro-ph/0302302] [INSPIRE].

[66] H.-W. Chiang, C.G. Boiza and M. Bouhmadi-López, *Observational constraints on generalised axion-like potentials for the late universe*, *JCAP* **08** (2025) 064 [arXiv:2503.04898] [INSPIRE].

[67] K. Choi, *String or M theory axion as a quintessence*, *Phys. Rev. D* **62** (2000) 043509 [hep-ph/9902292] [INSPIRE].

[68] H. Collins and B. Holdom, *Brane cosmologies without orbifolds*, *Phys. Rev. D* **62** (2000) 105009 [hep-ph/0003173] [INSPIRE].

[69] Y.V. Shtanov, *On brane world cosmology*, hep-th/0005193 [INSPIRE].

[70] G.R. Dvali, G. Gabadadze and M. Porrati, *4D gravity on a brane in 5D Minkowski space*, *Phys. Lett. B* **485** (2000) 208 [hep-th/0005016] [INSPIRE].

[71] C. Charmousis, R. Gregory, N. Kaloper and A. Padilla, *DGP specteroscopy*, *JHEP* **10** (2006) 066 [hep-th/0604086] [INSPIRE].

JCAP11(2025)018

[72] D. Gorbunov, K. Koyama and S. Sibiryakov, *More on ghosts in DGP model*, *Phys. Rev. D* **73** (2006) 044016 [hep-th/0512097] [INSPIRE].

[73] K. Koyama, *Ghosts in the self-accelerating universe*, *Class. Quant. Grav.* **24** (2007) R231 [arXiv:0709.2399] [INSPIRE].

[74] C. Deffayet, *Cosmology on a brane in Minkowski bulk*, *Phys. Lett. B* **502** (2001) 199 [hep-th/0010186] [INSPIRE].

[75] C. Deffayet, G.R. Dvali and G. Gabadadze, *Accelerated universe from gravity leaking to extra dimensions*, *Phys. Rev. D* **65** (2002) 044023 [astro-ph/0105068] [INSPIRE].

[76] S. Bag, S.S. Mishra and V. Sahni, *Emulating a ΛCDM-like expansion on the phantom brane*, *Phys. Rev. D* **97** (2018) 123537 [arXiv:1807.00684] [INSPIRE].

[77] A. Lue and G. Starkman, *Gravitational leakage into extra dimensions: probing dark energy using local gravity*, *Phys. Rev. D* **67** (2003) 064002 [astro-ph/0212083] [INSPIRE].

[78] J.B.R. Battat, C.W. Stubbs and J.F. Chandler, *Solar system constraints on the Dvali-Gabadadze-Porrati braneworld theory of gravity*, *Phys. Rev. D* **78** (2008) 022003 [arXiv:0805.4466] [INSPIRE].

[79] G. Dvali, A. Gruzinov and M. Zaldarriaga, *The accelerated universe and the moon*, *Phys. Rev. D* **68** (2003) 024012 [hep-ph/0212069] [INSPIRE].

[80] K. Koyama, *Cosmological tests of modified gravity*, *Rept. Prog. Phys.* **79** (2016) 046902 [arXiv:1504.04623] [INSPIRE].

[81] G.-B. Zhao et al., *Dynamical dark energy in light of the latest observations*, *Nature Astron.* **1** (2017) 627 [arXiv:1701.08165] [INSPIRE].

[82] J.J. Halliwell, *Scalar fields in cosmology with an exponential potential*, *Phys. Lett. B* **185** (1987) 341 [INSPIRE].

[83] F. Lucchin and S. Matarrese, *Power law inflation*, *Phys. Rev. D* **32** (1985) 1316 [INSPIRE].

[84] E.J. Copeland, A.R. Liddle and D. Wands, *Exponential potentials and cosmological scaling solutions*, *Phys. Rev. D* **57** (1998) 4686 [gr-qc/9711068] [INSPIRE].

[85] P.G. Ferreira and M. Joyce, *Structure formation with a selftuning scalar field*, *Phys. Rev. Lett.* **79** (1997) 4740 [astro-ph/9707286] [INSPIRE].

[86] B. Valeixo Bento, D. Chakraborty, S.L. Parameswaran and I. Zavala, *Dark energy in string theory*, *PoS* **CORFU2019** (2020) 123 [arXiv:2005.10168] [INSPIRE].

[87] M. Cicoli et al., *String cosmology: from the early universe to today*, *Phys. Rept.* **1059** (2024) 1 [arXiv:2303.04819] [INSPIRE].

[88] F. Apers et al., *String theory and the first half of the universe*, *JCAP* **08** (2024) 018 [arXiv:2401.04064] [INSPIRE].

[89] A.A. Sen and S. Sethi, *Quintessence model with double exponential potential*, *Phys. Lett. B* **532** (2002) 159 [gr-qc/0111082] [INSPIRE].

[90] T. Barreiro, E.J. Copeland and N.J. Nunes, *Quintessence arising from exponential potentials*, *Phys. Rev. D* **61** (2000) 127301 [astro-ph/9910214] [INSPIRE].

[91] V. Sahni and L.-M. Wang, *A new cosmological model of quintessence and dark matter*, *Phys. Rev. D* **62** (2000) 103517 [astro-ph/9910097] [INSPIRE].

[92] S.S. Mishra, V. Sahni and Y. Shtanov, *Sourcing dark matter and dark energy from α-attractors*, *JCAP* **06** (2017) 045 [arXiv:1703.03295] [INSPIRE].

JCAP11(2025)018

[93] S. Bag, S.S. Mishra and V. Sahni, *New tracker models of dark energy*, *JCAP* **08** (2018) 009 [arXiv:1709.09193] [INSPIRE].

[94] D. Rubin et al., *Union through UNITY: cosmology with 2,000 SNe using a unified Bayesian framework*, arXiv:2311.12098 [INSPIRE].

[95] D. Brout et al., *The Pantheon+ analysis: cosmological constraints*, *Astrophys. J.* **938** (2022) 110 [arXiv:2202.04077] [INSPIRE].

[96] DES collaboration, *The Dark Energy Survey: cosmology results with* ~ 1500 *new high-redshift type Ia supernovae using the full 5 yr data set*, *Astrophys. J. Lett.* **973** (2024) L14 [arXiv:2401.02929] [INSPIRE].

[97] W.L. Matthewson and A. Shafieloo, *Star-crossed labours: checking consistency between current supernovae compilations*, *JCAP* **01** (2025) 064 [arXiv:2409.02550] [INSPIRE].

[98] DESI collaboration, *DESI DR2 results. II. Measurements of baryon acoustic oscillations and cosmological constraints*, *Phys. Rev. D* **112** (2025) 083515 [arXiv:2503.14738] [INSPIRE].

[99] Y. Wang and P. Mukherjee, *Observational constraints on dark energy and cosmic curvature*, *Phys. Rev. D* **76** (2007) 103533 [astro-ph/0703780] [INSPIRE].

[100] P. Bansal and D. Huterer, *Expansion-history preferences of DESI DR2 and external data*, *Phys. Rev. D* **112** (2025) 023528 [arXiv:2502.07185] [INSPIRE].

[101] PLANCK collaboration, *Planck 2018 results. V. CMB power spectra and likelihoods*, *Astron. Astrophys.* **641** (2020) A5 [arXiv:1907.12875] [INSPIRE].

[102] ACT collaboration, *The Atacama Cosmology Telescope: DR6 gravitational lensing map and cosmological parameters*, *Astrophys. J.* **962** (2024) 113 [arXiv:2304.05203] [INSPIRE].

[103] J. Torrado and A. Lewis, *Cobaya: code for Bayesian analysis of hierarchical physical models*, *JCAP* **05** (2021) 057 [arXiv:2005.05290] [INSPIRE].

[104] R.E. Keeley, K.N. Abazajian, M. Kaplinghat and A. Shafieloo, *Preference for evolving dark energy from cosmological distance measurements and possible signatures in the growth rate of perturbations*, *Phys. Rev. D* **112** (2025) 043501 [arXiv:2502.12667] [INSPIRE].

[105] DESI collaboration, *Dynamical dark energy in light of the DESI DR2 baryonic acoustic oscillations measurements*, *Nature Astron.* (2025) [arXiv:2504.06118] [INSPIRE].

[106] D.H. Lee et al., *The shape of dark energy: constraining its evolution with a general parametrization*, arXiv:2507.11432 [INSPIRE].

[107] S. Bag, A. Viznyuk, Y. Shtanov and V. Sahni, *Cosmological perturbations on the phantom brane*, *JCAP* **07** (2016) 038 [arXiv:1603.01277] [INSPIRE].

[108] A. Viznyuk, S. Bag, Y. Shtanov and V. Sahni, *Versatile parametrization of the perturbation growth rate on the phantom brane*, *Phys. Rev. D* **98** (2018) 064024 [arXiv:1805.10405] [INSPIRE].

[109] L. Lombriser, W. Hu, W. Fang and U. Seljak, *Cosmological constraints on DGP braneworld gravity with brane tension*, *Phys. Rev. D* **80** (2009) 063536 [arXiv:0905.1112] [INSPIRE].

[110] R. Kallosh and A. Linde, *Universality class in conformal inflation*, *JCAP* **07** (2013) 002 [arXiv:1306.5220] [INSPIRE].

JCAP11(2025)018